Rochester Institute of Technology

RIT Digital Institutional Repository

Theses

8-2024

Energetics and Passivation of Surface Defects in HgTe Colloidal Quantum Dots

Jacob D. Eisensmith
jde4947@rit.edu

Follow this and additional works at: https://repository.rit.edu/theses

Recommended Citation

Eisensmith, Jacob D., "Energetics and Passivation of Surface Defects in HgTe Colloidal Quantum Dots" (2024). Thesis. Rochester Institute of Technology. Accessed from

This Thesis is brought to you for free and open access by the RIT Libraries. For more information, please contact repository@rit.edu.

Energetics and Passivation of Surface Defects in HgTe Colloidal Quantum Dots

A Thesis Towards the Completion of a Master of Science
in
Materials Science and Engineering

Jacob D. Eisensmith

School of Chemistry and Materials Science
Rochester Institute of Technology
Rochester, New York
August 2024

Signatures of Committee Approval:

The following indicates the approval and acceptance of the research presented.

Dr. Scott Williams Date

Materials Science and Engineering Graduate Program Director

Dr. Pratik Dholabhai Date

Thesis Advisor

Dr. Michael Pierce Date

Committee Member

Dr. Emiliano Brini Date

Committee Member

Dr. Ke Xu Date

Committee Member

Acknowledgements

The development of this thesis would not be possible without the contributions and mentorship of Dr. Pratik Dholabhai, my advisor. I was consistently empowered to seek out my own goals and curiosities, and he truly prioritized my learning and success. He has my sincere gratitude for sharing his resources, knowledge, and time. I would also like to thank the rest of my committee members, including Dr. Scott Williams, Dr. Michael Pierce, Dr. Emiliano Brini, and Dr. Ke Xu, each of whom have served as formative mentors and teachers. I wish all the best for the many friends I have met at RIT, including the faculty and staff within the School of Physics and Astronomy. I owe a great many thanks to them and my family for their unbridled support and kindness. And to Elise Weiss, to whom I owe my heart and inspiration, thank you for your confidence, dedication, and understanding. I'm finally done writing. For now.

Abstract

Colloidal quantum dots (CQDs), and especially HgTe CQDs, have the potential to disrupt traditional solid-state manufacturing of sensitive infrared photodetectors. Here we produce a surface model for (111) HgTe surfaces present in tetrahedral CQDs and attempt to use density functional theory (DFT) to explore various issues in the fabrication and performance of HgTe CQD photodetectors. One such concern is the presence of mid-gap trap states that can hurt device performance. In this work, we demonstrate that an abundant source of these trap states is unpassivated mercury at the surface of the nanocrystal, which can be corrected with passivation procedures. Furthermore, we are able to show that mercury vacancies, which contribute under-coordinated tellurium sites on the surface, do not appear to have an outsized impact on mid-gap states, unlike other II-VI CQD systems. This is likely a unique effect of the geometry of the tetrahedral nanocrystal. While tellurium vacancies were also explored, and preliminary results would indicate the presence of trap states, further simulation is warranted to verify this effect.

We are also able to demonstrate a universal control of conduction type in the CQDs regardless of the synthesis employed. The use of mercury substitution reveals the ability of indium species to induce n-type doping, while silver tends to accumulate on the FCC sites of mercury rich surfaces and induces p-type doping. We expect that experimental procedures can be devised to adapt many common syntheses to exploit this effect. Furthermore, we confirm the observation of a ligand dipole dependent Fermi level, highlighting the need for further investigation, and potentially enabling higher performing devices with shorter ligands and precisely engineered band alignments.

Table of Contents

List of Figures

Chapter I. A Brief Introduction to HgTe CQD Devices

Due to quantum confinement effects, colloidal quantum dots (CQCs) can exhibit size dependent band gaps, and provide a potential path to solution-based, highly tunable optoelectronic devices. Because of the large surface area to volume ratio, these structures are very surface dependent, allowing for a high degree of control over their electronic structure and conduction type. Recent investigations have suggested that silver chloride on the surface of HgTe quantum dots induced significant p-type doping and cited the use of $HgCl_2$ to passivate trap states [1]. In this work, we attempted to validate these claims through density functional theory (DFT) simulation of HgTe systems in the Vienna *Ab Initio* Simulation Package (VASP). Special attention was paid to the thermodynamic stability of substitutions and defects on the HgTe surface. Furthermore, the development of n-type doping is obtained with substitutional methods, suggesting a simple avenue for the development of PN-junctions within HgTe CQD layers.

This introductory chapter will provide a brief overview of solid-state physics as applicable to the results presented here and PN-junctions. Furthermore, the basic quantum mechanical principles and surface effects dominating a quantum dot will be discussed, and a widely adopted method of HgTe fabrication will be presented.

I.1 Solid-State Principles: From DOS to the Photodiode

It is well understood that the interaction between atomic orbitals that form molecules leads to the energy splitting of atomic orbitals into distinct molecular orbitals with higher energy “anti-bonding” and lower energy “bonding” states. Following the Aufbau principle, we should expect the bonding states to be filled with electrons first. When applied to bulk systems, or equivalently, a system periodic in real space and momentum or $\boldsymbol{k}$-space, this results in the manifestation of quasi-energy continuous bands. In semiconductor systems, there is a small finite energy separation between the highest occupied ground state and the lowest energy unoccupied excited state – the “band gap.” Plotting the molecular orbitals energy as a function of their wave vector ***k*** yields a band diagram which can be used to the evaluation of the band gap. In Kohn-Sham DFT, discussed in more detail in Chapter II, these molecular orbitals originate from the interaction of well-defined atomic orbitals, allowing for the “projection” of the atomic contribution onto particular molecular orbitals [2]. This will be used later in our analysis.

The density of states (DOS) results from the integration the available states of the molecular orbitals per unit energy over all ***k***-space. In practical terms, the available states with a given energy can be plotted as a 3D surface in ***k***-space, and the integration is reduced to summing the difference in surface area between surfaces separated by an infinitesimal energy. In the band gap, no states exist, and the resulting integral will be 0 states/eV. This provides another avenue for the determination of the band gap, and similar atomic orbital projections can be done to yield a projected-DOS or PDOS. For a more rigorous exploration of the fundamentals of band theory, the reader is directed to Kittel’s Introduction to Solid State Physics (8th ed. 2005), or McIntyre’s Quantum Mechanics (2012) referenced here [3, 4].

In traditional semiconductor device engineering, the picture is somewhat simplified. Rather than a quasi-continuous collection of orbitals, a typical “band diagram” is reduced to flat lines in real space representing the conduction band minimum (CBM) and valence band maximum (VBM) across the active device layers. At room temperature there will naturally be a small fraction of electrons that are promoted from the valence band into the conduction band, leaving positively charged available states, or holes. In pristine semiconductors, the electrochemical potential (or Fermi energy) of the Fermi distribution governing the statistical behavior of fermions is put in the center of the band gap to represent the equivalent number of electrons and holes in either band. This electrochemical potential can be tuned through a variety of methods, but substitution is the method most relevant here.

In semiconductor manufacturing, it is common for foreign atoms to be introduced to a semiconductor lattice either by direct ion beam exposure or thermal diffusion. Once within the lattice, “activated” dopants most often take the place of host atom sites. These dopants are specifically chosen to increase or decrease the ratio of electrons to holes, resulting in an n-type or p-type semiconductor, respectively. In a more fundamental sense, n-type dopants or donors contribute filled states very close to the CBM and require very little energy to liberate the electron into the continuous CBM states. Similarly, p-type dopants or acceptors introduce states near the VBM and can accept electrons from the valence band, preventing them from becoming mobile in the conduction band, and introduce holes. To represent this change in the relative number of charge carriers, the Fermi distribution is shifted by raising or lowering the electrochemical potential in n-type or p-type semiconductors, respectively.

When interfacing materials, the electrochemical potential must remain constant: in a PN junction where p-type and n-type semiconductors are interfaced, the electrochemical potential is left flat, which the CBM and VBM are shifted and bend to accommodate the transition. This band bending manifests as an electric field that empties a small “depletion region” around the junction of free carriers. In a PN photodiode, this strong electric field is exploited to extract excited photocarriers. Electrons in the valence band can absorb light matching or exceeding the band gap and be promoted into the conduction band, forming an exciton, or a bound quasiparticle. The electric field present in photodiodes is capable of quickly separating these charges, leading to a measurably elevated current through the device under proper irradiation.

I.2 Quantum Dot Films and HgTe

In the previous section we described a generic PN photodiode. Light that is absorbed by the photodiode must at least have an energy equal to the band gap of the junction material. With less energy, the light can simply be transmitted through the film with no detectable signal. In most cases for traditional semiconductors, this band gap is fixed. With scientific and consumer applications spanning the electromagnetic spectrum, plenty of materials science research is done to identify materials suitable for use in optoelectronics. IR sensitive films in particular are valuable for communications, astronomy, and spectroscopy techniques. Many of these films, including HgCdTe, InGaAs, and InP are fabricated with ALD and other slow vacuum processes that inflate cost [1]. By comparison, CQD films are often solution processed, allowing for active layers of devices to be made using high throughput fabrication techniques, significantly lowering costs.

Quantum dots exploit also quantum confinement to provide a size tunable band gap. Compared to bulk systems, an ideal CQD system would be able to span many regions of the electromagnetic spectrum by changing the growth conditions to yield different sized crystals. The main principle of this behavior is identical to the infinite wells commonly introduced in undergraduate quantum mechanics: the 1D infinite square well has eigenenergies inversely proportional to the square of the length of the well [4]. In a less abstract sense, quantum dots add a constraint to the dynamics of excitons, increasing the quasiparticle energy and expanding the band gap [5]. HgTe as a bulk material is a semimetal: its conduction band and valence band slightly overlap, leading some to say HgTe has a *negative* band gap. Quantum confinement through the fabrication of CQDs then is significant for HgTe as it allows for the tunable exploitation of the infrared spectrum.

I.3 HgTe CQD Devices and Potential Improvements

While HgTe is theoretically an ideal system for infrared applications, issues have emerged when attempting to make high performance IR photodiodes. In CQD systems, charge transport occurs through a charge hopping mechanism, rather than the band-like transport in bulk films [6]. The low mobility and highly localized states make the recombination of electrons and holes likely and reduces the overall efficiency of the device. To mitigate this, the extraction of charge and suppression of recombination current can be augmented with the use of an electron transport layer (ETL) [7]. The ETL effectively blocks the movement of holes, reducing the dark current, while providing a pathway for electrons to escape the CQD film and undergo fast band-like transport to the electrodes. Crucially, the alignment of the CBM of the CQD film and the ETL should closely match to ensure the efficient transmission of electrons. A similar hole transport layer (HTL) can also be incorporated into devices, but to our knowledge no such device has been made with HgTe CQDs, likely owing to its high CMB.

The precise alignment of the CBM/VBM for ETL and HTL layers in devices could be tuned through ligand engineering. CQDs are fabricated with surfactants and ligand species that hold the particles in suspension and these ligands are exchanged during the formation of the solid film. However, as demonstrated by Brown et. al the precise ligands used can have a profound impact on the alignment of the CBM/VBM [8]. A similar survey has not been performed for HgTe and its relevant ligands. While not heavily featured, work by Kroupa et. al also suggests that the choice of ligands can influence the relative position of the electrochemical potential within the CBM/VBM, indicating a potential effect on the effective doping of the CQD layer [9].

Effective tuning of the Fermi energy is imperative for the development of efficient PN junction diodes. An abundance of literature cites the p-type character of HgTe colloidal quantum dots, and many such cases use Ag_2Cl as an external p-type dopant source [1,7, 10, 11]. A cation exchange reaction with Ag_2Cl can be performed to convert the CQD layer into HgTe nanocrystals, releasing silver species into the surroundings and improving the p-type character, and the exact manifestation of silver-induced doping will be explored in Chapter VII. To supplement this, n-type films are sometimes formed through heterojunctions, but these introduce more synthesis optimization problems and band offset effects [10]. N-type character within HgTe nanocrystals has proven to be more elusive but has been demonstrated with unique syntheses [12]. However, this effect is tightly correlated to the size of the nanocrystal, and even changes the CBM/VBM positions of the film, further complicating the formation of a homojunction. This emphasizes the need for a more universal method for inducing n-type conduction within CQD layers: the use of indium species is most heavily explored in this work.

When constructing the model for a HgTe nanocrystal, many of the arguments are rooted in the crystal's synthesis. Throughout this work, a popular hot-injection method is assumed [13]. A solution of $HgCl_2$ is made with oleylamine at 100 °C. After choosing and reaching a reaction temperature, a solution of tri-octylphosphine telluride (TOPTe) and oleylamine is rapidly injected into the $HgCl_2$ solution, forming HgTe quantum dots suspended with oleylamine ligands. The dots are allowed to grow to a specific size, before quenching with a chloride solution. After casting the solution onto device layers, the films undergo a ligand exchange process to decrease the interdot distance and improve conductivity. This is most often done with ethanedithiol (EDT), although adding HCl and $HgCl_2$ to the ligand exchange solution has been shown to improve device performance [1]. The low reactivity of TOPTe compared to other tellurium precursors, and especially the readily reactive metal chloride precursors is well known [14]. With this understanding, it is assumed in this work that HgTe CQDs will primarily have mercury exposed surfaces. Furthermore, this hot injection technique frequently readily forms tetrahedral nanocrystals with {111} surfaces, which are modelled here in Chapter IV [13].

Chapter II. An Overview of Density Functional Theory

Density functional theory (DFT) is amongst the most powerful computational tools developed for materials science. The general concept is presented in this chapter, highlighting a few important fundamental equations as well as methods employed in the Vienna *Ab Initio* Simulation Package (VASP) simulations detailed in later chapters. In principle, DFT can serve as an *ab initio* technique, meaning any results are based on very few assumptions and come directly from physical law. For the simulation of materials like HgTe surfaces, this can be treated as solving the many-bodied Schrödinger equation (MBSE). As detailed below, this is very impractical in most cases, and a few important approximations are discussed to significantly reduce the computational complexity.

II.1 MBSE and the Born-Oppenheimer Approximation

The Schrödinger equation is often represented as $\widehat{H}\psi = E\psi$ where $\widehat{H}$ is the Hamiltonian matrix acting on the wave function ψ. The Hamiltonian operation on a wave function will return the total energy E as an eigenvalue of $\widehat{H}$. The Hamiltonian then is frequently constructed as a series of energy contributions. All materials are built up of atoms, which in turn can be deconstructed into nuclei and electrons. These components together will determine the energy components needed for a many-bodied Hamiltonian $\widehat{H}_{MB}$ that can determine the energy of any bulk system with a wave function Ψ: the kinetic energy of every electron and nucleus, and the Coulombic potentials between each electron-nucleus, electron, and nucleus pair. The full form of $\widehat{H}_{MB}$ is given in equation (1): note that electrons are indexed i, nuclei are indexed I, and the terms appear in order as listed above. Equation (1) is also expressed in “Hartree units” assuming the elementary charge $e = 1$, and the energy evaluated is given in Hartree: $E_{Ha} = \frac{e^2}{4\pi\epsilon_0 a_0}$.

$$\hat{H}_{MB} = -\sum_{i} \frac{\nabla_i^2}{2} - \sum_{I} \frac{\nabla_I^2}{2M_I} - \sum_{i,I} \frac{Z_I}{|\boldsymbol{r}_i - \boldsymbol{R}_i|} + \frac{1}{2}\sum_{i \neq j} \frac{1}{|\boldsymbol{r}_i - \boldsymbol{r}_j|} + \frac{1}{2}\sum_{I \neq J} \frac{Z_I Z_J}{|\boldsymbol{R}_I - \boldsymbol{R}_J|} \tag{1}$$

This Hamiltonian quickly becomes unwieldy at a computational level. Even with an impractical, small system evaluating the wave function at a few key points would still result in an unmanageably large Hamiltonian due to the repeated non-local evaluations of the Coulomb potential. Even for purely local calculations at one point, solving the eigenvalue equation means constructing a matrix whose size scales by $(N_i + N_I)^2$. For computational viability then, a series of approximations can be performed to reduce this many-bodied Hamiltonian into a series of local, single-bodied $N_i \times N_i$ Hamiltonians. To begin this process, we should recognize that there are substantial differences in the kinetic and potential energies of electrons and their nuclei. Due to their enormous mass relative to electrons, in a crystal system it is often a decent enough approximation to assume nuclei are fixed. In this scheme electrons first settle into their ground states, atomic positions may change slightly due to electrostatic forces, but the electrons can nearly instantaneously respond and occupy ground states that are not radically different from the original states. This separation of electron and nuclei dynamics is the Born-Oppenheimer approximation [15].

The Born-Oppenheimer approximation is sometimes presented as a decoupling of the electron and nuclear wave functions with separation of variables, but in this case, it is more practical to assume the nuclei to be fixed. The dynamics of the nuclei will be explored further in Chapter III but, in general, one does not need to consider nuclei to be quantum particles at all for simple relaxations. In the "clamped-nuclei" approximation then, the nuclear kinetic energy of $\widehat{H}_{MB} \to 0$ as the masses tend to infinity. Furthermore, the Coulomb potential between pairs of nuclei will also be unchanging. It is useful then to remove this energy from the Hamiltonian, evaluate purely the electronic contribution, then add the nuclear potential back as a global correction. To finish eliminating the invocation of nuclear coordinates $\boldsymbol{R}$ we can recognize that the potential experienced by the electrons from the nuclei now only depends on the electronic coordinates $\boldsymbol{r}_i$, allowing equation (2) to be substituted into $\widehat{H}_{MB}$. Finally, we can present the many-*electron* Hamiltonian in equation (3).

$$\sum_i V_n(\boldsymbol{r}_i) = -\sum_{i,I} \frac{Z_I}{|\boldsymbol{r}_i - \boldsymbol{R}_I|} \tag{2}$$

$$\widehat{H}_{ME} = -\sum_i \frac{\nabla_i^2}{2} + \sum_i V_n\,(\boldsymbol{r}_i) + \frac{1}{2}\sum_{i \neq j} \frac{1}{|\boldsymbol{r}_i - \boldsymbol{r}_j|} \tag{3}$$

II.2 Independent Electrons and Towards Hartree-Fock

Equation (3) describes a collection of electrons that strongly interact via the Colomb force. While being independent of nuclear dynamics, it still maintains a degree of non-locality by summing over dissimilar electrons. Further approximations made by Hartree [16], Slater [17] and Fock [18] lend themselves to the optimization of the Hamiltonian by eliminating this non-locality. We can take the first step by assuming that the electrons are independent, and do not see the direct Coulombic interaction of every other electron. Attempts to correct this rough approximation will follow, but here we can now say that the Hamiltonian in equation (3) is merely the sum of a series of single electron Hamiltonians. This implies that in some way we can represent the many-bodied wave function Ψ as a series of independent electron wave functions $\phi_j(\boldsymbol{r}_i)$. The exact separation of ϕ_j is intuitively captured in a Slater determinant, as written in equation (4). By separating out ϕ_j in this way, the Pauli exclusion principle can be abided: swapping electrons between two states results in a change of sign in Ψ.

$$\Psi = \frac{1}{\sqrt{N!}} \begin{vmatrix} \phi_1(\boldsymbol{r}_1) & \dots & \phi_1(\boldsymbol{r}_N) \\ \vdots & \ddots & \vdots \\ \phi_N(\boldsymbol{r}_1) & \dots & \phi_N(\boldsymbol{r}_N) \end{vmatrix} \tag{4}$$

A natural consequence of this formulation is that the total (electronic) energy E is the sum of the eigenenergies ε of each of the independent electron states. In addition, the probability of finding an electron at a position $\boldsymbol{r}$ then becomes the inner product of its occupied state at position $\boldsymbol{r}$. Taken to the extreme, the charge density $n(\boldsymbol{r})$ is then the probability of finding any electron at position $\boldsymbol{r}$, or the sum of all independent probabilities at $\boldsymbol{r}$. This charge density is critical to density functional theory, as will be explored later. However more immediately it allows us to start correcting the purely independent approximation. For instance, we can generalize the Coulomb potential from each foreign electron as an average. Generically, we can describe the potential of a charge density through Poisson's equation [19]. The solution written here in equation (5) is again in Hartree units, is the Hartree potential, and can be added into the Hamiltonian alongside $V_n(\boldsymbol{r})$.

$$V_H = \int \frac{n(\boldsymbol{r}')}{|\boldsymbol{r} - \boldsymbol{r}'|} d\boldsymbol{r}' \tag{5}$$

Combined with the independent electron Schrodinger equation and the determination of the charge density, the evaluation of the Hartree potential forms a self-consistent loop in the Hartree-Fock equations. This is the basis of the self-consistent field (SCF) problem: the wave functions ϕ_i must yield a charge density that results in the correct Hartree potential to again return ϕ_i. However, the formulation of the Hartree-Fock equations is not yet complete. Namely, in the independent electron Schrodinger equation, we should recognize that we have not imposed that the energy be minimized with respect to the wave functions ϕ_i, and the Pauli exclusion principle further stipulates that these states should be orthogonal to prevent occupation of states with identical eigenvalues. With such a scheme, Fock derived the Hartree-Fock independent electron Schrödinger equation, given in equation (6) [18]. This formulation effectively removes the projection of all other electron states ϕ_j from ϕ_i, ensuring orthogonality. Ultimately, the Hartree-Fock equations are limited by the re-introduction of non-locality into the Schrodinger's equation with the evaluation of an integral over $\boldsymbol{r'}$.

$$\left[-\frac{\nabla^2}{2} + V_n(r) + V_H(r)\right]\phi_i(r) - \int \phi(r')\sum_j \frac{\phi_j^*(r')\phi_j(r)}{|r-r'|}dr' = \varepsilon_i\phi_i(r) \tag{6}$$

II.3 Kohn-Sham Equations and Density Functional Theory

The central idea to DFT is that the ground state energy of the system is purely a functional (or a scalar function of a function) of the electron density. This is already hinted at in the Hartree-Fock equations above: only the last exchange potential term does not explicitly invoke the charge density, since the kinetic energy is dependent on the wave function and therefore the charge density. This concept is known as the Hohenberg-Kohn theorem and was more rigorously argued by proving that the charge density n uniquely determines the nuclear potential V_n, and therefore Ψ [20]. Instead of assuming the total electronic energy was minimized with the independent electron orbitals then, Kohn and Sham enforced that the total electronic energy be minimized with the charge density $n(\boldsymbol{r})$ explicitly. Practically speaking, this allowed them to evaluate the total electronic energy with largely independent and local energies, summed with an unknown exchange and correlation energy $E_{xc}[n]$. This functional remains unknown and describes the discrepancy between the independent and many-electron models. The Kohn-Sham equations, and their dependencies which complete the SCF, are given in equations (7a-7e) [21].

$$\left[-\frac{1}{2}\nabla^2 + V_n(\boldsymbol{r}) + V_H(\boldsymbol{r}) + V_{xc}(\boldsymbol{r})\right]\phi_i(\boldsymbol{r}) = \varepsilon_i\phi_i(\boldsymbol{r}) \tag{7a}$$

$$V_n(r) = \sum_I \frac{Z_I}{|r - R_I|} \tag{7b}$$

$$\nabla^2 V_H(r) = -4\pi n(r) \tag{7c}$$

$$V_{xc}(r) = \frac{\delta E_{xc}[n]}{\delta n} \tag{7d}$$

$$n(r) = \sum_i |\phi_i(r)|^2 \tag{7e}$$

Ultimately, DFT as presented in the Kohn-Sham equations offers a perfect *ab initio* approach to a system of many electrons, but the lack of a known exchange-correlation potential prevents its ideal performance. Instead, many functionals are given as empirical or theoretical approximations. The local density approximation (LDA) for instance evaluates the theoretical exchange energy and empirical correlation energy of a homogenous electron gas in discrete volume elements of the total electron density [21]. The generalized gradient approximation (GGA) in general improves over LDA by incorporating dependence on the gradient of the charge density. The work presented here is done exclusively with the Perdew-Burke-Ernzerhof (PBE) exchange and correlation functionals. The PBE functionals improve over previous GGA functionals in that they are purely grounded in theory (rather than fit empirically to one system) and only rely on two fundamental constants [22].

While PBE functionals are widely used in DFT for materials science and condensed matter studies for their broad applicability, all non-perturbative Kohn-Sham based DFT methods are well known to underestimate the optical band gap. This is intuitive with the understanding that DFT, which relies on the Hohenberg-Kohn theorem, is only valid for the ground state of electrons; excitations are beyond the scope of the proof [20]. More rigorously, we can consider the band gap to be the energy difference of the topmost occupied state ε_V and the bottommost unoccupied state ε_C. Ideally, in an equivalent expression, we can evaluate the electronic band gap as the difference between the ionization energy and electron affinity, as shown in equation (8) [21].

$$E_g = \varepsilon_C - \varepsilon_V = (E_{N-1} - E_N) - (E_N - E_{N+1}) \tag{8}$$

In the Kohn-Sham formulation of DFT, there is a subtle difference between the two expressions in equation (8). While the difference in energy between the neutral and ionized systems is large and sufficiently calculable for small systems, in bulk systems with $\sim 10^{23}$ electrons, this difference in energy is exceedingly small, such that we should evaluate equation (8) in the $\Delta n \rightarrow 0$ limit. Ultimately, the difference between the two expressions in equation (8) when using the Kohn-Sham equations is the difference in the exchange and correlation functionals as $\Delta n \rightarrow 0$. Many formulations of LDA and GGA functionals are continuous, prohibiting the evaluation of this subtle difference and resulting in catastrophic underestimations of the band gaps of semiconductors and insulators. While corrections to the band gap exist, they will not be rigorously explored here. As a qualitative demonstration, DFT with Hubbard-like corrections (DFT+U) is shown in Chapter V.

II.5 VASP as a DFT Package

The previous sections have described, heuristically, the mechanics of DFT. The Viena *ab initio* Simulation Package (VASP) is a robust commercial application capable of applying the Kohn-Sham equations, solving the SCF loop, and determine the independent electron orbitals ϕ_i. This section will briefly discuss the particulars of VASP and its calculations. While Chapter III will cover ionic relaxation and the movement of nuclei independent of electrons, this section aims to clarify the construction of the wave functions ϕ_i. Fundamentally, a Fourier transformation can decompose a given function in real space into plane waves of an arbitrary parameter space [19]. In this case, it is most useful to move into momentum or $\boldsymbol{k}$-space. We can construct the "plane-wave basis" which maintains periodicity in $\boldsymbol{k}$ and $\boldsymbol{r}$ in equation (9).

$$\phi_{i,\boldsymbol{k}}(\boldsymbol{r}) = \sum_{\boldsymbol{G}} c_{\boldsymbol{kG}} \exp(i(\boldsymbol{k}+\boldsymbol{G})\boldsymbol{r}) \tag{9}$$

Equation (9) suggests that the wave functions for a particular value of $\boldsymbol{k}$ are summations of plane waves that span a momentum space $\boldsymbol{G}$, which corresponds to a sum of higher frequency an energy plane waves in real space. It is often impractical to construct perfect representations of electron orbitals with plane waves, so some approximations are introduced. The one parameter that is both easily available to VASP users and important to energetic convergence is the "cut-off energy" or the highest magnitude of $\boldsymbol{G}+\boldsymbol{k}$ allowed into the summation of equation (9). The pseudopotentials included with VASP have a default value ENMAX, and in this work the cut-off energy was left above this value at 300 eV to ensure convergence and comparability between calculations [23]. Furthermore, the evaluation of core electron states and other states with high frequency oscillatory behavior, the evaluation of $\phi_{i,\boldsymbol{k}}(\boldsymbol{r})$ would mandate the summation of many more states than necessary for smoother, more chemically relevant states. The solution, as presented by Kresse and D. Joubert, is to slightly adapt the projector augmented-wave (PAW) method to the plane wave basis [2].

$$|\Psi_n\rangle = |\tilde{\Psi}_n\rangle + \sum_i (|\phi_i\rangle - |\tilde{\phi}_i\rangle)\langle\tilde{p}_i|\tilde{\Psi}_n\rangle \tag{10}$$

Equation (10) above describes the all-electron (AE) wave function Ψ_n in the PAW scheme. Central to the PAW method is the concept of a PAW sphere; within some critical radius around an atomic site, the true AE wave function begins to deviate from the pseudo-wave function denoted with the tildes. Within this radius, the pseudo-wave function is corrected by a projector function $\tilde{p}_i$ and it is identical to the AE wavefunction outside of this radius. By employing the pseudo-wave function and projector function, the AE solution can be approximated with considerably fewer plane waves. Additionally, one can assume that electrons within the PAW sphere are tightly bound to the nucleus and will not change in position or energy much when considering nuclear orbitals. The frozen-core approximation then assumes these electrons to have their wave functions fixed, and instead screen the nuclear charge [24]. In the frozen-core PAW scheme there are effectively 3 key sources of charge density: point charges due to nuclei, the fixed charges within the PAW sphere due to the pseudo-wave function, and the accurate charge outside of the PAW sphere. To correct the multipole within the PAW sphere, some compensation charge is introduced when evaluating the charge density. The pseudopotential then, as implemented in VASP is description of the Hartree, exchange and correlation functionals that depend on the pseudo-wave function charge and the compensation charge.

Chapter III. Ionic Relaxation

In the previous chapter we have established how DFT is used to obtain the total energy of a system through the relaxation of the electronic structure. Until this point, it has proven useful to consider the nuclei as fixed. However, the Coulombic forces generated by the electrons and neighboring nuclei on a particular nucleus are likely not zero in the first iteration. We could then choose to move the nuclei in a particular path that relates to this force, in the hope that the energy will further decrease towards a ground state. Choosing the path along which nuclei travel is not trivial, and many such algorithms exist. In this chapter, we will introduce a method using conjugated gradients, which is most similar to the proprietary method employed in VASP in later chapters.

III.1 Forces on Nuclei

In the scheme discussed previously, our nuclei were assumed to be fixed; this allowed us to neglect their kinetic energy and let us calculate a total energy assuming the Coulombic potential between nuclei to be constant. These arguments are still useful, and when determining the electronic configuration, they will still be in place. When determining nuclear forces however, the coulombic potential especially will have an outsized role. From classical mechanics, we understand the force $\boldsymbol{F}$ at point $\boldsymbol{d}$ to be related to the potential energy U:

$$\boldsymbol{F} = -\frac{\partial U}{\partial \boldsymbol{d}} \tag{1}$$

Determining this derivative with respect to every change in nuclear positions with the nuclear Hamiltonian from the Born-Oppenheimer approximation is inherently time consuming since the derivative of the electronic energy with respect to every shift in nuclear positions would need to be calculated. It would be helpful to instead consider the entire many bodied Hamiltonian, reprinted here for convenience:

$$\hat{H} = -\sum_{i}\frac{\nabla_i^2}{2} - \sum_{I}\frac{\nabla_I^2}{2M_I} - \sum_{i,I}\frac{Z_I}{|\boldsymbol{r}_i - \boldsymbol{R}_I|} + \frac{1}{2}\sum_{i\neq j}\frac{1}{|\boldsymbol{r}_i - \boldsymbol{r}_j|} + \frac{1}{2}\sum_{I\neq J}\frac{Z_I Z_J}{|\boldsymbol{R}_I - \boldsymbol{R}_J|} \tag{2}$$

Notice that only two terms in the Hamiltonian will change with respect to the nuclear coordinate $\boldsymbol{R}_I$: the Coulombic interaction between nuclei and electrons, and the Coulombic interaction between nuclei. This is directly analogous to $\frac{\partial U}{\partial \boldsymbol{R}_I}$ since it lacks any terms contributing to kinetic energy. We can now quickly attempt to evaluate the derivative of the total energy, or the expectation value of the Hamiltonian. This derivative can be with respect to any useful variable, but $\boldsymbol{R}_I$ is most useful here.

$$\frac{\partial E}{\partial \boldsymbol{R}_I} = \frac{\partial}{\partial \boldsymbol{R}_I}\int \psi^* \hat{H}\psi \, d\boldsymbol{r} = \int \frac{\partial \psi^*}{\partial \boldsymbol{R}_I}\hat{H}\psi + \psi^*\hat{H}\frac{\partial \psi}{\partial \boldsymbol{R}_I} + \psi^*\frac{\partial \hat{H}}{\partial \boldsymbol{R}_I}\psi \, d\boldsymbol{r} \tag{3}$$

Since $\hat{H}\psi = E\psi$, the first and second terms can be combined via the product rule. The derivative will cause the combined term to vanish, since the integral is constant via normalization. This means that $\frac{\partial E}{\partial \boldsymbol{R}_I} = \int \psi^* \frac{\partial \hat{H}}{\partial \boldsymbol{R}_I} \psi \, d\boldsymbol{r}$, which is generally true for any derivative [25]. Below is the derivative of the Hamiltonian with respect to $\boldsymbol{R}_I$. We can determine the forces on a given nucleus by negating the expectation value of this derivative.

$$\frac{\partial \hat{H}}{\partial \boldsymbol{R}_I} = -\sum_{i}\frac{Z_I(\boldsymbol{r}_i - \boldsymbol{R}_I)}{|\boldsymbol{r}_i - \boldsymbol{R}_I|^3} + \sum_{J\neq I} Z_I Z_J \frac{\boldsymbol{R}_J - \boldsymbol{R}_I}{|\boldsymbol{R}_J - \boldsymbol{R}_I|^{\boldsymbol{3}}} \tag{3}$$

$$\boldsymbol{F}_I = -\left\langle \psi \left| \frac{\partial \hat{H}}{\partial \boldsymbol{R}_I} \right| \psi \right\rangle = Z_I\left[\int n(\boldsymbol{r})\frac{\boldsymbol{r} - \boldsymbol{R}_I}{|\boldsymbol{r} - \boldsymbol{R}_I|^3}\, d\boldsymbol{r} - \sum_{J\neq I} Z_J \frac{\boldsymbol{R}_J - \boldsymbol{R}_I}{|\boldsymbol{R}_J - \boldsymbol{R}_I|^{\boldsymbol{3}}}\right] \tag{4}$$

This result indicates that the forces on a given nucleus are only due to the classical electrostatic interaction between itself and the surrounding electrons and nuclei. These forces will be the starting point of our ionic relaxation.

III.2 The Line Search

Fundamentally, when minimizing a multidimensional function (like a 3-dimensional energy surface) is a series of line searches – or minimizations in a specified direction along the multidimensional function. When starting a search in DFT, we cannot know exactly what the energy landscape $f(x)$ is, but we do have key starting points of information: the energy at the starting ionic positions $f(x_0)$ in 1 dimension, and the forces $-f'(x_0)$. Using this information, we can surmise whether to search in the $+x$ or $-x$ direction depending on the sign of $f'(x)$. The issue now is that we cannot know how far to search to successfully locate the minimum. In VASP this is solved manually: the length of the first "trial step" in a line minimization is scaled by the user with the POTIM parameter [26].

We now have two points: x_0 and an arbitrary guess x_1, which is based on the sign of $f'(x_0)$. To evaluate $f(x_1)$ is to reevaluate the total energy of the system i.e., go through the self-consistent electronic relaxation as covered in Chapter II. This computational limitation is why developing fast, and reliable minimization algorithms is incredibly important for materials science research, and especially when using DFT. However, as covered in the previous section, the evaluation of the energy $f(x_1)$ provides the forces $-f'(x_1)$ with relative ease. As a result, we have gained two key pieces of information with one self-consistent cycle. Collectively, $f(x_0)$, $f(x_1)$, $f'(x_0)$, and $f'(x_1)$ allow us to determine a better guess for what the minimum in the x direction might be.

In describing the oscillations of atoms around their equilibrium bond lengths, we use a parabolic approximation to describe their potential energy in one dimension. It makes sense then that we could do something similar here. The standard form of the quadratic $g(x) = ax^2 + bx + c$ has three parameters. We can solve these parameters by letting $g(x_1) = f(x_1)$, $g'(x_0) = f'(x_0)$, and $g'(x_1) = g'(x_1)$. With these conditions, we have created a system of three linear equations which can be easily solved with, for example, Cramer's rule. Our next best guess for the minimum of $f(x)$ is the minimum of this parabola. This system is demonstrated in Figure 3.1.

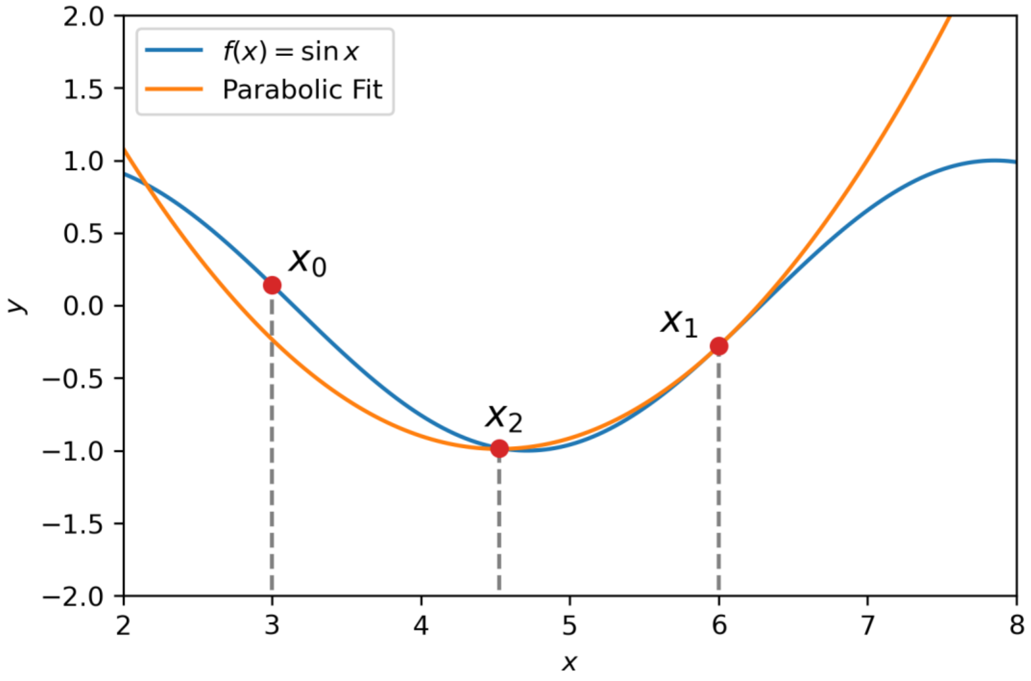

Figure 3.1 An example energy surface with initial guess x_0, "trial step" x_1, and the parabolic interpolation of the two. The minimum position of the parabola is the next "corrector step" x_2.

It is important to note however that we are only enforcing one constraint on the actual value of $g(x)$. This means that $f(x_0)$ is not necessarily equal to $g(x_0)$. In cases where $f(x_0) \neq g(x_0)$ the best-case scenario is that we have wasted a data point and produced a subpar estimation for the minimum, as demonstrated in Figure 3.2. In the worst case however, this can lead to an estimation for the minimum that falls outside the bounds of the local potential well, which could result in the simulation relaxing into a metastable state. To prevent this scenario then, when $f(x_0) \neq g(x_0)$ it might make sense to use a cubic approximation, where all four (two energetic, two sets of forces) points of reference are utilized. In solving, this is can be done in a similar manner to the parabolic case, but with a 4x4 matrix when using Cramer's rule:

$$\begin{bmatrix} x_0^3 & x_0^2 & x_0 & 1 \\ x_1^3 & x_1^2 & x_1 & 1 \\ 3x_0^2 & 2x_0 & 1 & 0 \\ 3x_1^2 & 2x_1 & 1 & 0 \end{bmatrix} \begin{bmatrix} a \\ b \\ c \\ d \end{bmatrix} = \begin{bmatrix} f(x_0) \\ f(x_1) \\ f'(x_0) \\ f'(x_1) \end{bmatrix} \tag{5}$$

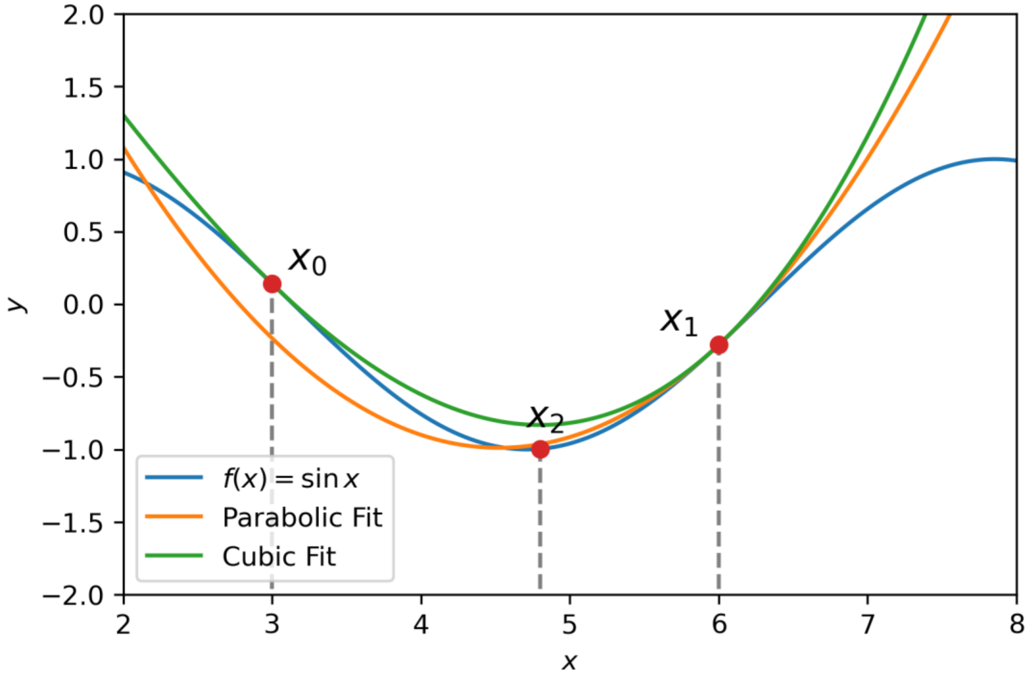

Figure 3.2 The energy surface, x_0 and x_1 are consistent with Figure 3.1. The point x_2 however is moved to the minimum of the cubic fit, which utilizes all energy and force data available.

Our next best guess x_2 is the local minimum of either the parabolic or cubic fit using x_0 and x_1. This can simply be found using $g'(x) = 0$ which necessitates solving a linear or quadratic equation. After determining x_2, we can then evaluate $f(x_2)$ and $f'(x_2)$ through another self-consistent cycle. With a set of function evaluations and their derivatives, we now have a wealth of information at our disposal. Provided x_2 is not the minimum of $f(x)$ or close to within some tolerance, we have enough information to enter a variation of Brent's algorithm that takes the derivatives into account.

Brent's algorithm uses a set of points (x_0, x_1) that bind the minimum. The point x_2 should lie within this interval and yield the lowest value of $f(x)$ of the three. For the sake of our example in Figures 3.1 and 3.2, these conditions were met, but if this is not the case some preliminary reindexing can occur. In a traditional Brent's algorithm scheme, new points are assumed using a parabolic interpolation of the three points, similar to the procedure above. Unlike the above case, with three points, the parabola should be uniquely identified. With the addition of derivative information, however, we can likely improve our performance. For instance, the signs of the derivatives at each point will uniquely determine which inner interval $[x_0, x_2]$ or $[x_2, x_1]$ the minimum lies in [27]. The minimum is also the point in this uniquely determined interval where $g'(x) = 0$. This means we can use robust root finding methods, like the secant method, where the new point x_3 is determined by a linear interpolation of the derivatives:

$$x_3 = x_2 - f'(x_2)\frac{x_2 - x_{0/1}}{f'(x_2) - f'(x_{0/1})} \tag{6}$$

The second term in equation (6) is the change between x_{i+1} and x_i, and can serve as a measure of convergence; ideally this distance should continually decrease [27]. If this is not the case, Brent's algorithm defaults to a slower, more guaranteed minimum finding algorithm. Figure 3.3 demonstrates the next guess x_3 given through this algorithm. This procedure is then simply repeated until the minimum of $f(x)$ is obtained within some tolerance.

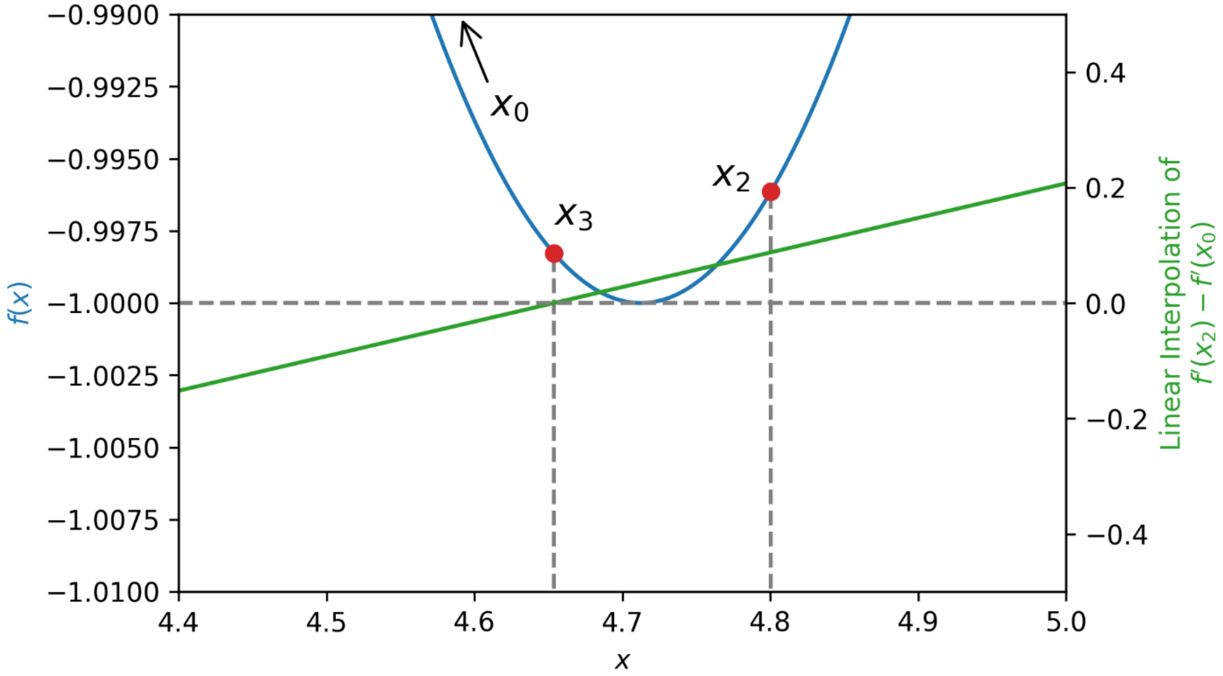

Figure 3.3 The small region of the energy surface $f(x)$ is plotted. Based on the signs of $f'(x_0)$, and $f'(x_2)$, a minimum must exist between the region, and a linear interpolation of the derivatives is made. The point where this interpolation is zero becomes the new guess x_3.

III.3 Successive Search Directions and Conjugated Gradients

At this point, we have taken what essentially amounts to one step in our ionic relaxation process, even though we needed to determine the total energy of the system 3 or more times. While this first step minimized the force exerted on a given nucleus in the direction indicated by the starting gradient $-\nabla E$, the force overall is not likely to be minimized. Initially, it feels intuitive that the next search direction should be along the new energy gradient. This method would be considered a "method of steepest descent." While this method will bring the system towards convergence, we can demonstrate that it is likely not the most efficient way of doing so. Indeed, given that we minimized the force along this initial gradient, the new gradient felt by the nucleus must be (within some tolerance) orthogonal to the previous one. This is true of every repeated step, implying that we must take repeated steps along the same few orthogonal directions to reach the minimum of an elliptical parabolic well [27].

We can imagine a better method that only steps in a given search direction $\boldsymbol{h}_i$ once. With some finite n number of directions, the algorithm would perfectly converge after n steps. To generate a series of orthogonal basis vectors, we would nominally use the Gram-Schmidt process. A series of orthogonal search vectors however would be identical to the steepest descent case: the negative gradients $\boldsymbol{g}_i$ are already orthogonal. Instead, we can imagine a quadratic matrix representation of the energy landscape $f \approx c + \boldsymbol{b} \cdot \boldsymbol{x} + \frac{1}{2}\boldsymbol{x} \cdot \mathbf{A} \cdot \boldsymbol{x}$. In truth, our search directions should be **A-**orthogonal or conjugate, meaning $\boldsymbol{h}_i \mathbf{A} \boldsymbol{h}_j = 0$ to guarantee convergence to a minimum in the energy landscape [28]. The set of conjugate search directions given by Fletcher and Reeves is as follows:

$$\boldsymbol{h}_{i+1} = \boldsymbol{g}_{i+1} + \beta_i \boldsymbol{h}_i$$

Here β_i is the remaining conjugate Gram-Schmidt coefficient after considering the linearly independent vectors to instead be the negative gradients $\boldsymbol{g}_i$. For the parabolic approximation of $f(\boldsymbol{x})$ denoted above, it has many equivalent derivations, but each may progress differently depending on the exact form of $f(\boldsymbol{x})$. Polak and Ribiére proposed the form in equation (8), which can reduce to zero, restarting the conjugation procedure [29].

$$\beta_i = \frac{(\boldsymbol{g}_{i+1} - \boldsymbol{g}_i) \cdot \boldsymbol{g}_i}{\boldsymbol{g}_i \cdot \boldsymbol{g}_i}$$

The ionic relaxation procedure can now be summarized. The initial ionic positions loaded into the POSCAR goes through electronic relaxation, and an initial total energy and set of ionic forces are obtained. The ions are allowed to shift in the direction given by the initial force vectors by an amount scaled by POTIM, and the energies and forces are recalculated. This new set of points is used in a parabolic or cubic fit to determine a likely minimum, and the energies and forces are recalculated at that estimate. If necessary, further line searches through a derivative based version of Brent's algorithm proceed. When the forces in the initial direction are minimized, a new direction determined through the conjugate gradients method is used, and the cycle continues until the difference in total energy between two ionic steps is below EDIFFG [30].

Chapter IV. Development of the Surface Model

The study of fully realized nanocrystals with density functional theory proved to be inherently difficult. To an extent, this is to be expected. The VASP software package used here is a plane-wave DFT suite utilizing methods described in Chapter II. Plane-wave methods rely on periodicity in the unit cell, which is automatically introduced with VASP. If we wanted to isolate a cluster of atoms, such as in a HgTe nanocrystal, we must introduce some vacuum space into the unit cell itself to minimize interactions between the simulated cluster and the assumed copies that exist along each of the lattice directions $(\mathbf{a}, \mathbf{b}, \mathbf{c})$. Furthermore, ideally one would simulate enough atoms to build a nanocrystal with relevant optoelectronic properties. In our case, tetrahedral SWIR sensitive HgTe nanocrystals might have an edge size of 10 nm, or about 4300 atoms. Combined, an extremely large unoptimized vacuum spacing and thousands of atoms each with 6 or 12 simulated electrons makes for an exceptionally complicated system. We argue here that a surface model is a more tenable solution.

IV.1 Initial Simulation of a Nanocluster

Initially undeterred by the computational difficulty of nanocluster simulation, we developed a Python package capable of reading and writing VASP POSCAR files which describe the positions and types of each atom in the unit cell, along with the lattice vectors. In our initial approach, we elected to generate $N \times 3$ ion position arrays beginning with a unit cell POSCAR as an input. Included as a part of this Crystal Generation Utilities (CGU) package was a relatively fast method for developing large bulk systems by replicating this unit cell using a parallelized layer-wise method. A tetrahedral supplement was added to the CGU to allow for this bulk system to be trimmed into $\{111\}$ tetrahedra. Ultimately, the CGU multiprocessing method was overbuilt for the small (~0.27 nm) crystal systems needed. However, auxiliary functions added simple vector movements, atomic layer parsing, and other functionality that made the CGU invaluable for quickly making edits to POSCAR files.

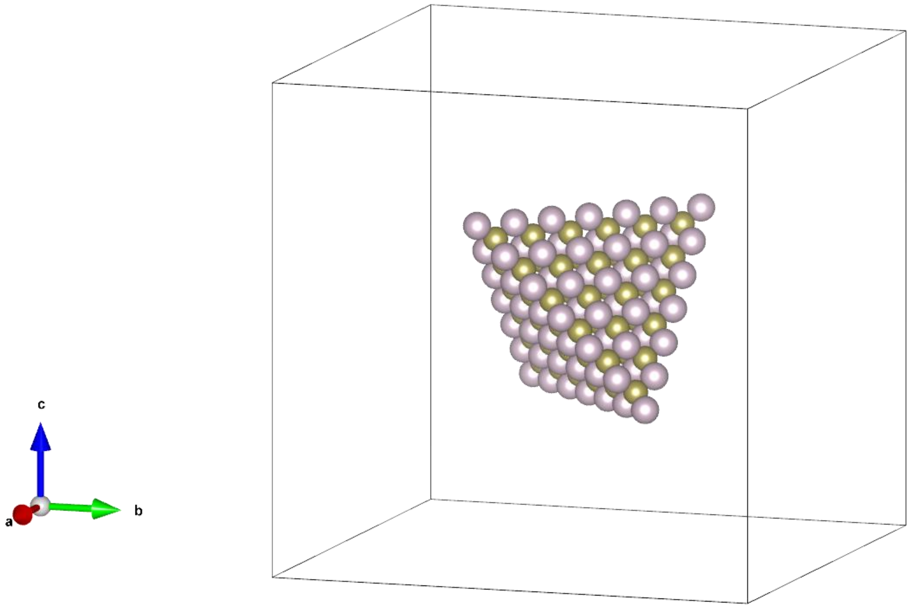

Figure 4.1 Generated tetrahedral HgTe structure with a Hg-facing surface. This model was assumed based on fabrication methods discussed in Chapter I.

Using the CGU, we generated a tetrahedral nanocrystal with a 27-angstrom edge size, or 140 atoms shown in Figure 4.1 above. The structure was generated with simple cubic lattice vectors with a cell parameter of approximately 54.8 nm. With the tetrahedron centered, the distance between edges of the simulated structure and its assumed periodic copies was 3.54 nm. This is potentially far more than necessary, but ultimately the smallest needed distance was not optimized. When starting a DFT simulation in VASP, the initial charge density in the unit cell is assumed to be a superposition of each atom's atomic charge density. This poor guess at the initial charge density necessitated 43-44 blocked Davidson steps to establish the initial charge density with which to *begin* ionic relaxation. Ultimately, only two to three complete ionic steps were allowed to complete in the maximum allowed 24-hour runtime, which is potentially less than one complete line search (see Chapter III). Because these runs were terminated prematurely, full charge density output files would not be recorded. Similarly, wave function output files meant for restarting successive runs were disabled due to limited disk space. As a consequence, to continue ionic relaxation for another 24 hours would have necessitated the extremely long optimization of the initial charge density. For this reason, no fully relaxed structure was generated, and we re-examined the simulated system.

IV.2 Initial Surface Model Generation

Surface states on a quantum dot system have an outsized impact on their properties due to their extremely large surface area to volume ratio. As we will later demonstrate, the qualitative trends that can be observed through modification of a colloidal quantum dot surface can then be observed using a simple surface model rather than the full isolated nanocrystal. This method has precedent in literature, being used to study the effects of different ligand polarizations on the band alignment of quantum dot films [8]. Some limitations on this method are the loss of complete 3-dimensional confinement and the asymmetry in surfaces generated with HgTe; without modification, a Hg-facing and a Te-facing surface is shown in the method described below. The mitigation of these issues is described later in this chapter.

HgTe in the bulk phase can be described as a diamond structure with cubic lattice vectors. Experimentally, it is understood that HgTe nanocrystals fabricated with high temperature hot-injection techniques will display {111} surfaces [13]. The <111> direction by definition cannot be described by one of the cubic lattice vectors and necessitates some transformation of our unit cell. The transformation matrix that was most useful to us is given in equation (1), and the new cell vectors are visualized in Figure 4.2.

$$(\mathbf{a}', \mathbf{b}', \mathbf{c}') = (\mathbf{a}, \mathbf{b}, \mathbf{c}) \begin{bmatrix} P_{11} & P_{12} & P_{13} \\ P_{21} & P_{22} & P_{23} \\ P_{31} & P_{32} & P_{33} \end{bmatrix} = (\mathbf{a}, \mathbf{b}, \mathbf{c}) \begin{bmatrix} 1 & 0 & 0 \\ 0 & 1 & 0 \\ 1 & 1 & 1 \end{bmatrix} = (\mathbf{a} + \mathbf{c}, \mathbf{b} + \mathbf{c}, \mathbf{c}) \qquad (1)$$

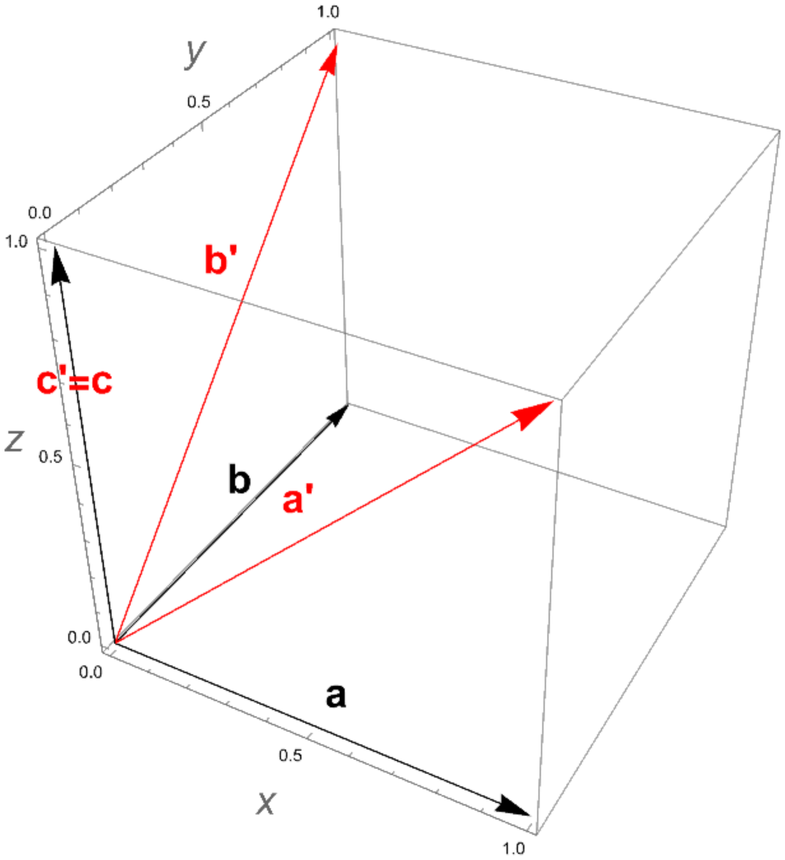

Figure 4.2 Visualization of the original cubic lattice vectors and the transformed vectors with a tetrahedral surface normal to $\mathbf{b}'$ *and* $\mathbf{c}'$.

We can see that the plane spanned by $\mathbf{b}'$ and $\mathbf{c}'$ is the $(\overline{1}\overline{1}1)$ plane, which is equivalent to (111) with a 180° rotation about *z* and is indeed present on the tetrahedra previously simulated (see Figure 4.1). After this transformation, the unit cell was transformed into a 2x2x4 supercell, such that the simulated structure had 4 AB (HgTe) layers. This final structure included 64 atoms of either species for a total of 128, and the final $\mathbf{c}'$ lattice vector was extended by 2.5 nm to isolate the slab when considering periodicity. This simulated structure is given in Figure 4.3. Of note is that the two surfaces on either side of the structure are different. To preserve the stoichiometry within the slab, each Hg layer must be accompanied by a Te layer. In such a configuration, to consider a Hg-facing layer the Te-facing layer must also be included. For the determination of surface energy, as will be demonstrated in the next section, this is not an issue. However, for calculations of electronic structures, this will need to be accounted for.

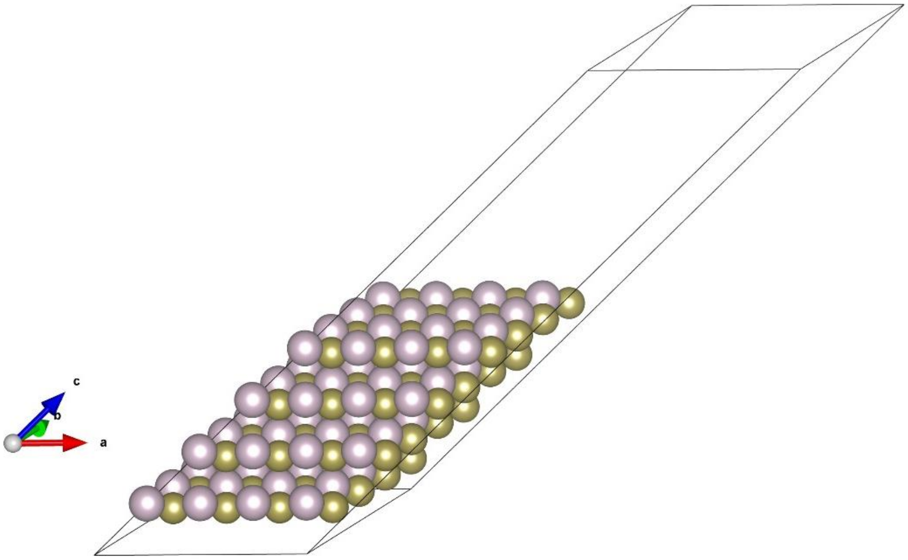

Figure 4.3 Final simulated structure with 4 HgTe layers and a vacuum region that defines the surface.

IV.3 Surface Energy and Initial Electronic Structure

The 4 layer unpassivated surface was allowed to fully relax using the conjugate gradients method described in Chapter III. In their bulk configuration, atoms are arranged such that they have the lowest potential energy and are their most stable. Intuitively, there must be an energy associated with the cleaving of a bulk material and exposing a surface to, in this case, a vacuum. DFT is well suited to calculating the surface energy σ, as denoted in equation (2) [31]. The surface energy is normalized to $2A$, representing both of the slab's surfaces, where A in this case is the area of the parallelogram formed by surface atoms.

$$\sigma = \frac{1}{2A}(E_{slab} - nE_{bulk}) \tag{2}$$

Here E_{bulk} is the calculated energy of a bulk material, and n denotes the equivalent number of units of the bulk material in the slab. Our comparison was made to a bulk 2x2x2 supercell, meaning there are $n = 2$ units in the slab. By determining the fully relaxed structure to have energy $E_{slab} = -223.2795$ eV, the single surface energy was evaluated as 2.850 J/m^2. However, as noted above, the slab as constructed has two distinct surfaces. To accommodate this asymmetry, Tian et al. proposed a “cleaving energy” method [32]. Equation (3) describes the simplest form of the method. The cleaving energy E_C is the energy associated with removing the slab from the bulk, without any surface relaxation taking place: it is the difference between a fully frozen slab E_F and the bulk. This energy is assumed to be evenly distributed across the two surfaces, and this is a reasonable assumption for compounds whose constituent elements have similar electronegativities [32]. The relaxation energy of surface i, $E_{R,i}$ is the difference between (one half of) the cleaving energy and the energy of the slab when only the subject surface is allowed to relax $E_{r,i}$. This is achieved through Selective Dynamics in the POSCAR file [33]. Finally, the surface energy can be determined through the difference between the cleaving energy and the relaxation energy of the subject surface. Fundamentally, the cleaving energy method isolates the energy of forming a particular surface by removing the effects associated with an asymmetric relaxation.

$$\sigma_i = E_C - E_{R,i} = \frac{1}{A}\left(E_F + E_{r,i} - 2nE_{bulk}\right) \tag{3}$$

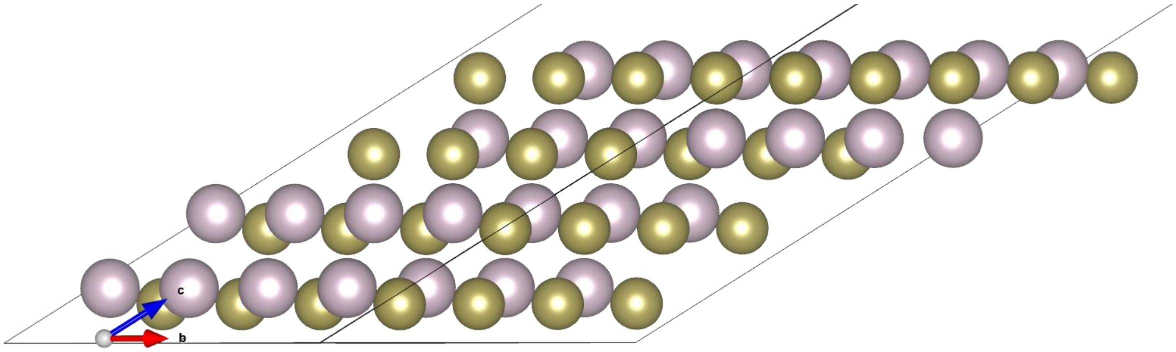

Figure 4.4 Side profile of the fully relaxed 4 layered structure.

Using this method and equation (3), the surface energy of the Hg-facing surface was determined to be 2.735 J/m^2, which is not too dissimilar to the original value of 2.850 J/m^2. Qualitatively, this could be explained by considering the relaxation of the Hg-facing and Te-facing surfaces at the top and bottom of Figure 4.4, respectively. The Hg-facing layer shows an appreciable change in the angle between Hg and neighboring Te atoms just beneath the surface when compared to the bulk. However, this same effect is not observed in the Te-facing layer, implying that the relaxation energy of the Te-facing surface may be small enough to not skew the surface energy obtained by the single surface model too significantly. While the energetics of the HgTe surface have not been significantly explored previously, the majority of this work is concerned with the electronic structure of the slab system, which is being used to model the quantum dot.

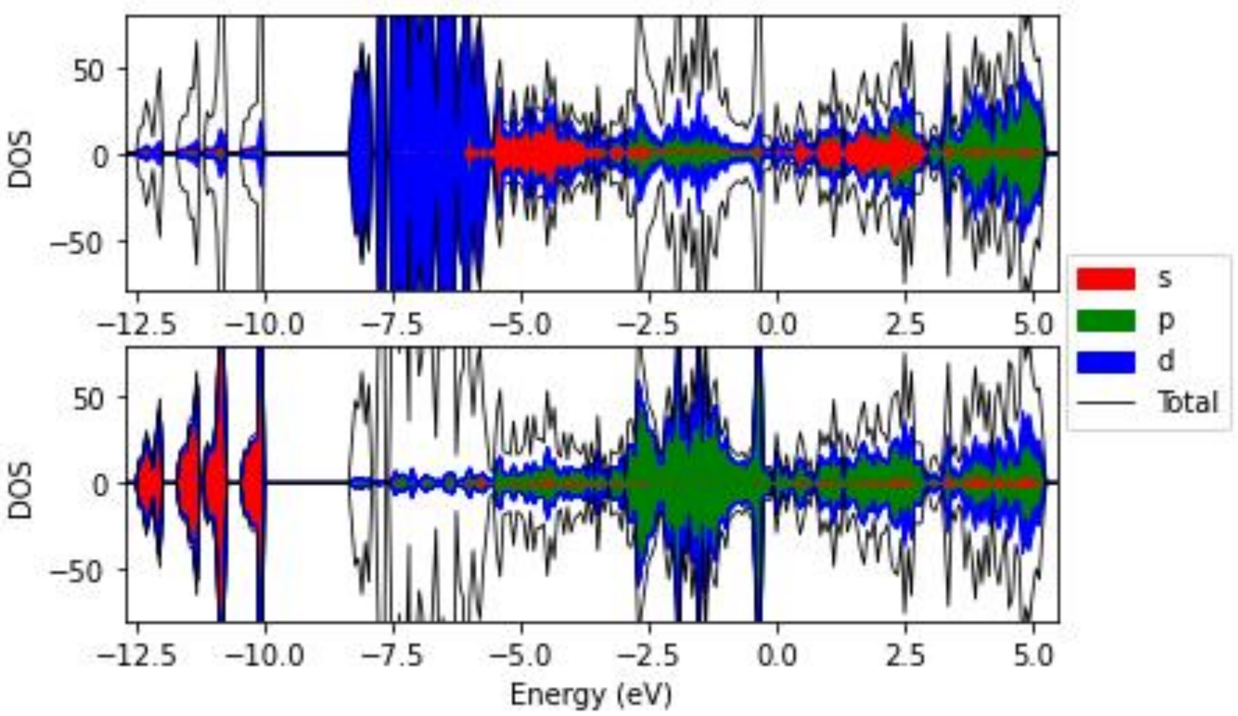

Figure 4.5 DOS plots of the entire spectrum of the 4 layered HgTe slab. The Hg (top) and Te (bottom) contributions are plotted independently. Energies are given relative to the Fermi energy.

The initial electronic structure, and in particular the density of states (DOS), of the 4 layered slab system is shown in Figure 4.5. While the entire spectrum is given in Figure 4.5, going forward we will focus entirely on the states within 2 eV of the Fermi energy. Based on the Te projections, the *s*-orbital contributes most strongly to the low energy core bands separate from the rest of the electronic structure. The most significant contribution to these bands from the mercury atoms are the diffuse *d*-orbitals. The *d*-orbitals also dominate the spectrum below -6 eV. Around the Fermi energy we can make a few more observations. Immediately noticeable is the lack of the band gap around the Fermi energy. The *p*-orbitals in the Te projection contribute significantly to both the valence and conduction bands. This will be more thoroughly explored in later chapters when band diagrams are presented, but this shared contribution can be attributed to bands primarily from tellurium that bridge an otherwise positive band gap. The small overlap in the conduction and valence bands gives HgTe it is colloquial “negative” band gap. However, the nanosheet simulated here should show considerable quantum confinement effects, giving rise to a positive band gap like in the nanocrystal case. The “band gap problem” with DFT discussed in Chapter II makes the vanishing band gap in this case very likely. However, there are still more considerations we could make. For instance, surface states and dangling bonds with energies near the Fermi level could fill the otherwise clear band gap. Additionally, while we initially simulated 4 AB layers since they terminate most similarly (i.e. a Hg-Te pair in the top layer identical to that of the bottom layer through periodicity) further quantum confinement, and a growth in the band gap, can be achieved by limiting the slab to 3 or fewer layers.

Chapter V. Correction to the Implemented Surface Model

During the evaluation of the effects of mercury vacancies in Chapter VI, after all the simulations presented here were completed, we noticed that the trap states apparently induced were very close to the valence band. This would make HgTe somewhat defect tolerant, since the defect states could very easily allow for holes to escape, and less likely to behave as recombination sites in optoelectronic applications. It also naturally urges the investigation of Te vacancies to see if there would be a more pronounced effect. Such a realization would be significant, since previous studies suggest that under-coordinated chalcogen sites, rather than metals, are the most likely contributors to surface traps in II-VI semiconductors [34]. To investigate this, a structure with a tellurium vacancy was produced and allowed to relax using the quasi-Newton algorithm. Concurrently, a structure with 3 AB HgTe layers was made, and the Hg-facing surface was passivated with Z=1.5 pseudohydrogens. The Te-facing layer was left unpassivated, essentially reversing the passivation first introduced in Section VI.1. This structure originally was not considered since, compared to HgCl, the tellurium precursor trioctylphosphine telluride is much less reactive, making a Hg-rich surface much more likely, as mentioned in Chapter I.

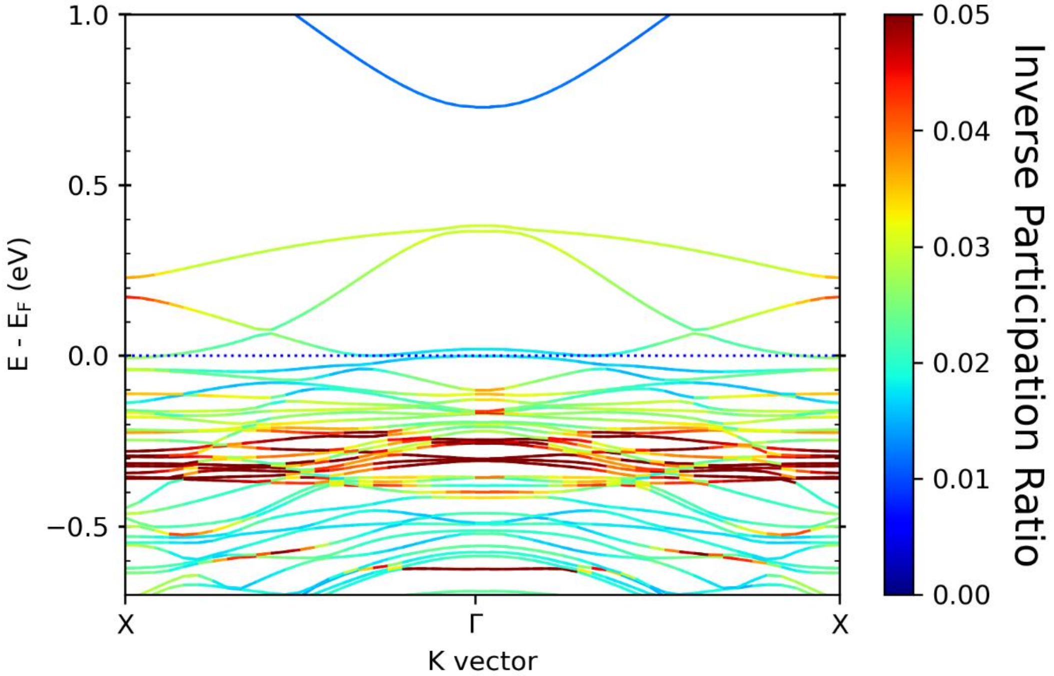

Figure 5.1 Band diagram of the unpassivated tellurium surface superimposed with the inverse participation ratio of the bands.

Figure 5.1 shows the band diagram of the structure with an unpassivated tellurium surface. The bands are colored by the "inverse participation ratio" (IPR). The IPR is a normalized figure that represents the weight of a molecular orbital on a particular atom; it ranges from 1 at the atomic orbital limit, and 1/N representing an entirely delocalized band distributed over all N atoms. The band diagram in Figure 5.1 demonstrates that the bands above the Fermi level are unoccupied surface states. This intuitively makes sense since, from an oxidation state perspective, we would expect mercury to donate electrons and reduce tellurium to Te^{-2}. Interestingly, the removal of the passivating pseudohydrogens fully restores spin-symmetry in the band diagram. The introduction of spin-asymmetry with the Z=1.5 pseudohydrogens on the tellurium surface is not well understood. Furthermore, we note the existence of a strong band gap, ranging from the top of the surface states to the bottom conduction band, or about 0.4 eV. This made the possibility of filling or otherwise eliminating the tellurium surface states attractive, leading to further investigations. Using pseudohydrogens was already attempted to dubious effect in Chapter VI, so regular Z=1 hydrogens were added. While breaking the stoichiometry of the slab was avoided up until this point, using pseudohydrogens has proven effective at passivating mercury associated surface states. In a second trial then, a mercury layer was added below the unpassivated tellurium, which itself was passivated with 3x16 pseudohydrogens to retain the tetrahedral coordination.

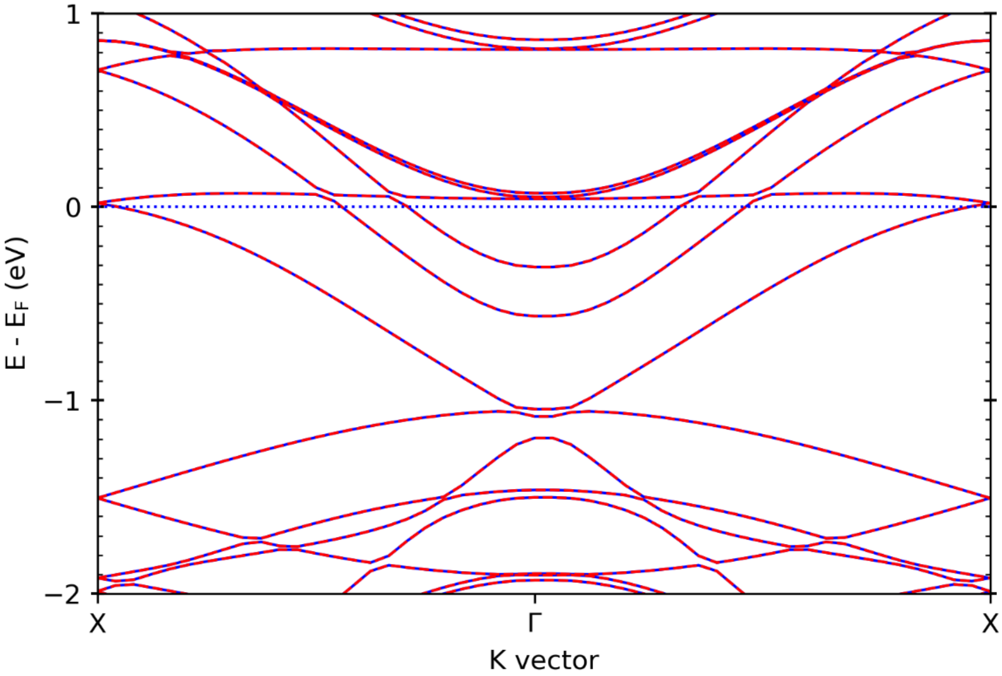

Figure 5.2 Band diagram of the structure with a hydrogen passivated Te-facing surface.

The attempted passivation to “fill” the surface states resulted in band diagrams more familiar to bulk HgTe, with a small band inversion at the Γ-point. While the Te-passivating hydrogen solution drew the Fermi level far into the conduction band, the structure with a passivating mercury layer, as depicted in Figure 5.3b, places the Fermi level predicably at the valence band maximum. Note that in the band diagram above, symmetry was disabled in the supercell, which likely resulted in the artifacts near band crossings. These simulations also do not result in any spin-asymmetry, suggesting that any splitting is not linked to the passivation of Te-facing layers, but instead to the interaction between exposed Te surfaces and Z=1.5 pseudohydrogens specifically. The DOS plots of these trials bear some resemblance to the 3-layered HgTe structure used throughout this work, as demonstrated in Figures 5.3a and 5.3b. Below the Fermi level, the down-spin states are similar, and the same is true for up-spin states above the Fermi level.

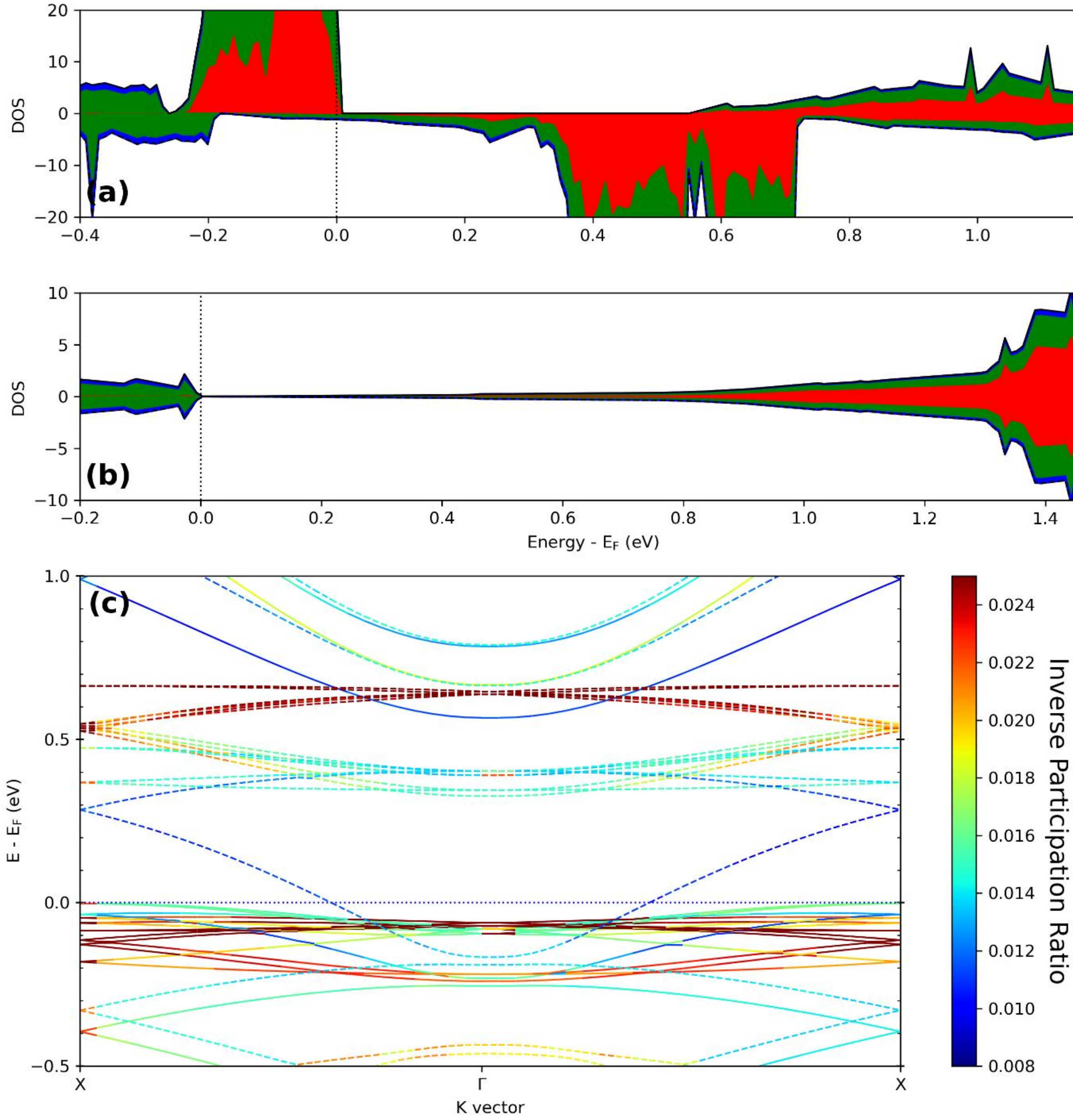

Figure 5.3 DOS plots for (a) the base 3-layered HgTe model and (b) the mercury passivated Te-facing layer. The band diagram (c) highlights the most localized states in deep red.

This realization prompted the examination of the IPR of the bands in the base 3-layered HgTe model, shown in Figure 5.3c. The color scaling is intentionally dramatic; bands with an IPR corresponding to localization to <40 atoms are pushed to the top of the scale. Immediately apparent is that, barring what appears to be simple energy splitting between the same band with opposite spins, the down-spin states below the Fermi level, and the up-spin states above the Fermi level are the most delocalized states. This matches the asymmetric behavior noted in the DOS plots and suggests that the down-spin (up-spin) states below (above) the Fermi level are related to the surface interactions between Te and pseudohydrogens, rather than the true conduction or valence band. This behavior is even hinted at in Figure 6.4 where the atomic projections of the bottom AB layer of HgTe make up the vast majority of what we now understand to be spin-asymmetric surface states.

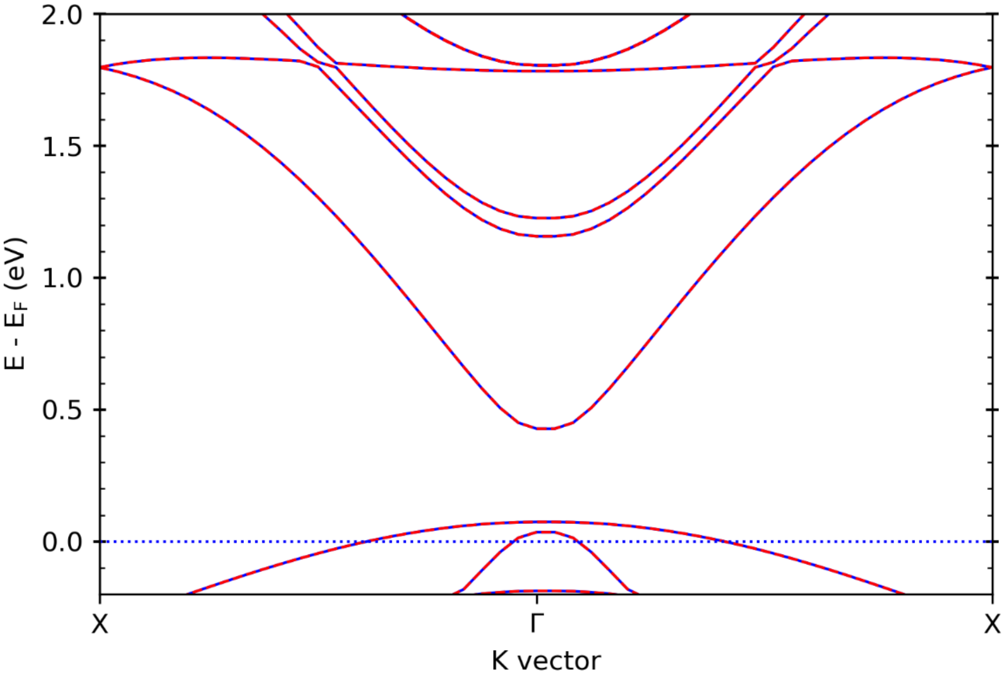

Figure 5.4 Band diagram of the new, mercury passivated structure when using DFT+U, where $U = 8.4$ *eV.*

When considering the lack of a band gap first noticed in Chapter IV, one of the first methods thought of to induce separation in the bands was a Hubbard parameter *U* to restore the electronic gap expected in the confined HgTe system. This has some precedent in studying HgCdTe quantum wells [35]. We elected a rather large *U* parameter of 8.4 eV that would act on the *d*-orbitals of mercury. With this simple correction, we were able to demonstrate a considerable band gap with the mercury passivated model. The Fermi level in this case falls just below the valence band edge, indicating innate p-type behavior. This could likely be tuned by the choice of *U* and should be investigated further.

Ideally, the calculations presented elsewhere in this document should be performed with the excess-Hg passivation method demonstrated above. Utilizing DFT+U would also allow for less ambiguous investigations of mid-gap states caused by vacancies. However, many of the qualitative observations made here remain valid. Bands introduced through Hg substitutions align with a theoretical understanding of acceptor and donor states, have the “correct” spin for their position relative to the Fermi level, and the substitution successfully nullifies electrical effects due to the Hg vacancy. Furthermore, the shifts in Fermi level demonstrated through ligand substitution agree well with surface dipole trends and previous studies concerning the effect. Care should be taken however regarding the effects of mercury vacancies. While the bands introduced around the Fermi level due to the vacancy do appear to elevate the Fermi level, they are still up-spin states which could correspond to a relation between these states and the Te-H interaction states. To solve this, the atomic orbital projections of the top two layers of atoms were taken and are presented in Figure A.5.

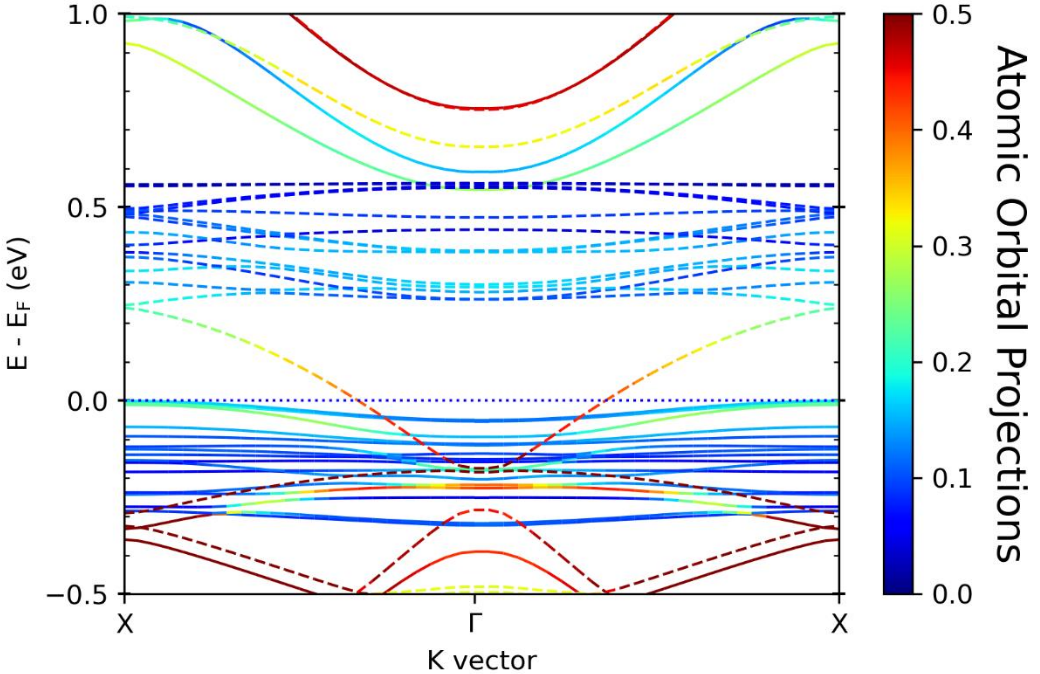

Figure 5.5 Band diagram of the Hg vacancy structure, with atomic orbital projections highlighting the two AB layers closest to the defect site.

The projections demonstrate that the up-spin states close to the Fermi level are disproportionally weighted to atoms other than the top two atomic layers, which includes the defect site. We can conclude then that it is likely related to the Te-H interaction. However, the valence band and states just beneath it, including select up-spin bands, do show a large share of top-layer character. These states could constitute acceptor states, as noted in the main text. This, and the geometry of a tetrahedral nanocrystal that makes 2-coordinated Te sites less likely compared to less strongly-faceted geometries, provides some evidence that tetrahedral {111} HgTe nanocrystals should be somewhat tolerant of Hg vacancy defects, and instead develop more p-type conduction.

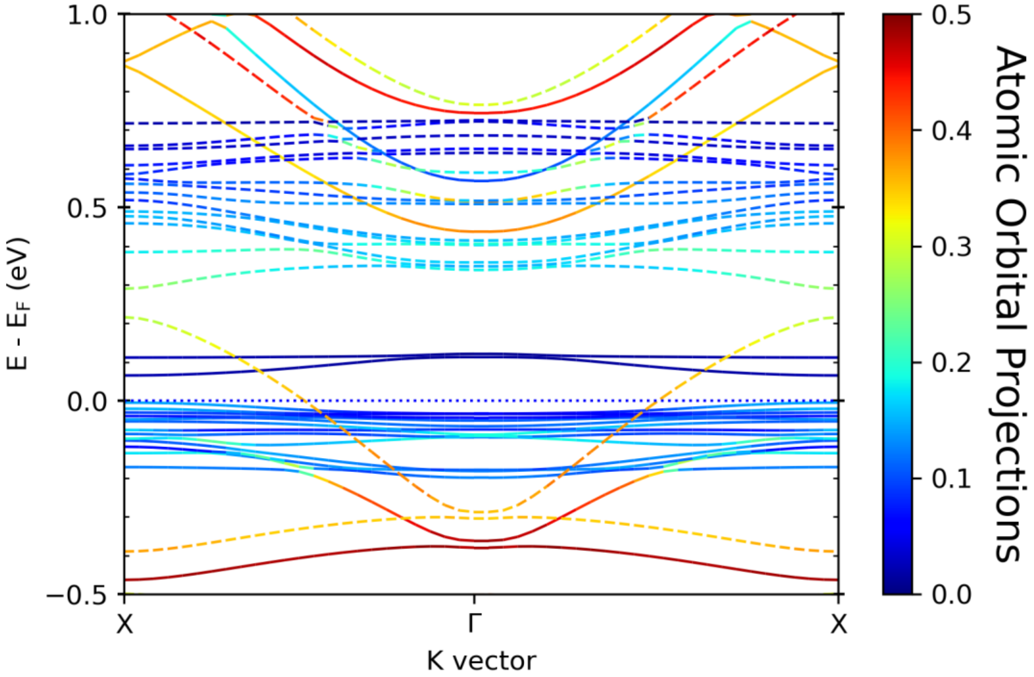

Figure 5.6 Band diagram of the Te vacancy structure, with atomic orbital projections highlighting the top two AB layers (which does not include the Te-facing surface).

The tellurium vacancy, mentioned at the beginning of this section but not yet discussed, is more ambiguous. Figure 5.6 shows a similar projection to that of Figure 5.5, but for the tellurium vacancy structure. As expected, most of the flat, down-spin bands around the Fermi level are not related to the atomic orbitals of the top two layers of atoms. The states nearest to the Fermi level have evidently shifted up relative to the true conduction/valence down-spin bands. However, there are two up-spin bands that appear to be the conduction/valence bands shifted down in energy. This makes assigning vacancy states around a theoretical band gap dubious, since it’s unclear if the bands are merely spin shifted, in which case neutral tellurium vacancies have no discernible impact around the Fermi level, or if a true vacancy band exists that crosses between the conduction and valence bands, with catastrophic effects to IR sensitive HgTe CQDs. Further investigation, particularly with an appropriately passivated system, is warranted.

Chapter VI. Surface and Defect Model Electronic Structures

In Chapter IV, we discussed the initial electronic structure obtained for a 4 AB (HgTe) layered structure. In particular, we noted that no band gap was achieved. As a potential remedy, the density of states (DOS) and band diagrams for n-layered structures will be explored. Having $n < 4$ should lead to increased confinement effects and lead to a wider separation between the conduction and valence bands. Furthermore, the initial structure simulated displayed surface relaxation, and dangling bonds on the surfaces of the slab could be contributing to states around the Fermi energy, potentially bridging the band gap. This allows for comparisons between bare surfaces and those with single- and double-sided passivation techniques. Ultimately, we find that while a positive band gap in many-layered HgTe (111) surfaces does not appear, the monolayer form does have a positive band gap. We can utilize the trends with decreasing layer counts to make assumptions about the effects of modifications to the (111) surfaces on colloidal quantum dots. The first of these studies presented here is that of a surface mercury vacancy.

VI.1 Passivation of (111) HgTe Surfaces

The first attempts made at achieving a positive band gap in our structures were through passivation. The simulated (111) HgTe slab is isolated by a vacuum region on either side of the cell through periodic boundary conditions. The slab, separated from a bulk material, must theoretically break bonds that would have otherwise been at the slab's surface. This rearrangement of charge density at the surface can manifest as dangling bonds, which typically have energies close to that of the Fermi energy. This makes any potential dangling bonds a prime candidate for hiding an otherwise already narrow band gap. To begin exploring this issue then, pseudohydrogens were added to the tellurium facing surface. While the relaxation of this surface was shown to involve considerably less energy than that of the mercury surface, we assumed that the mercury-facing surface would be most likely to be realized experimentally due to the relative reactivities of the mercury and tellurium reactants. Since the VASP pseudopotential of tellurium models six electrons (2s and 4p) and we assume these to be equally shared across the four tetrahedral bonds in the diamond HgTe lattice, we selected a pseudohydrogen with Z=1.5, though this proved to be a suboptimal approach, as noted in Chapter V.

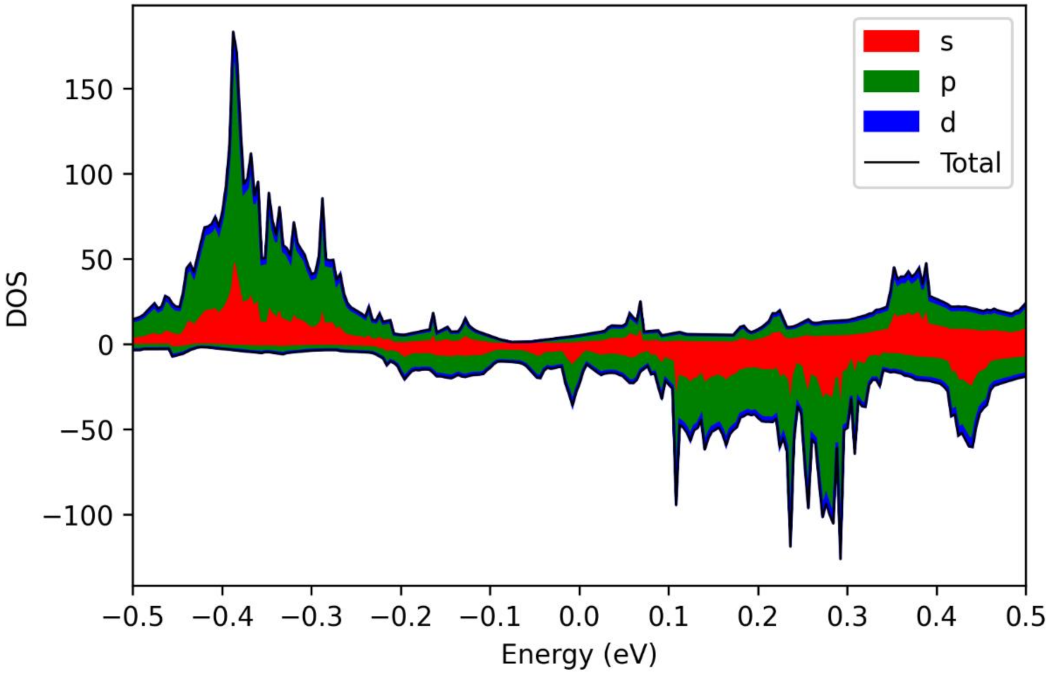

Figure 6.1 Density of states of the 4 AB layered structure with Te-facing passivation.

The DOS of the tellurium-passivated structure again does not have a band gap. We should note that in the previous chapter where we presented a DOS plot of the entire spectrum of an unpassivated slab, we had Gaussian smearing enabled. This smearing calculates the band energies (and in turn, the DOS) at each k-point by assuming the occupation of a Kohn-Sham eigenstate to be, in this case, Gaussian about the eigenenergy. For metals with many bands around the Fermi energy, this can reduce the effects of bands alternating from above and below the Fermi energy and preventing electronic convergence [36]. The tetrahedral method with higher order (Blöchl) corrections instead divides a k-point mesh into tetrahedra, calculates the energies at the vertices, and interpolates the eigenenergies between them. The tetrahedral method prevents charge sloshing since the energy is calculated by integrating the interpolation, rather than the step function about the Fermi energy [37]. Furthermore, this method has been shown to improve the overall accuracy of energy calculations when not using *k*-mesh optimization. For this and future DOS plots then, the tetrahedral method with higher order corrections was used.

In the tellurium-passivated structure, special attention was paid to two features: a broad peak centered around –0.15 eV, and another peak around 0.07 eV. In Chapter IV we noted a continuum of states and attributed them to primarily a band with primarily tellurium behavior. This band, which exists with or without passivation and is mentioned in Chapter V, contributes to the down-spin states. For that reason, our analysis here is limited to the up-spin states. To demonstrate that these states around the Fermi level are indeed a result of states originating on the surface of the slab, a series of projections on the DOS were calculated. These projections considered the slab as layers, with projection 1 being the passivated bottommost Te-facing layer and projection 4 being the unpassivated topmost Hg-facing layer. Projections 1 and 4 are given in Figure 6.2. While the bottommost layer of HgTe contributes strongly to the presumed up-spin dominated conduction band and down-spin dominated valence band, the topmost layer sees notable increases in the DOS around the features of interest, which suggests that these states are indeed local dangling bond states. When considering a HgTe nanocrystal then, it is important to recognize that even pristine stoichiometric surfaces are prone to developing traps near the Fermi level. This effect could be more pronounced in colloidal systems which are initially passivated and held in suspension with large organic ligands whose steric hinderance could limit the overall passivation of a quantum dot.

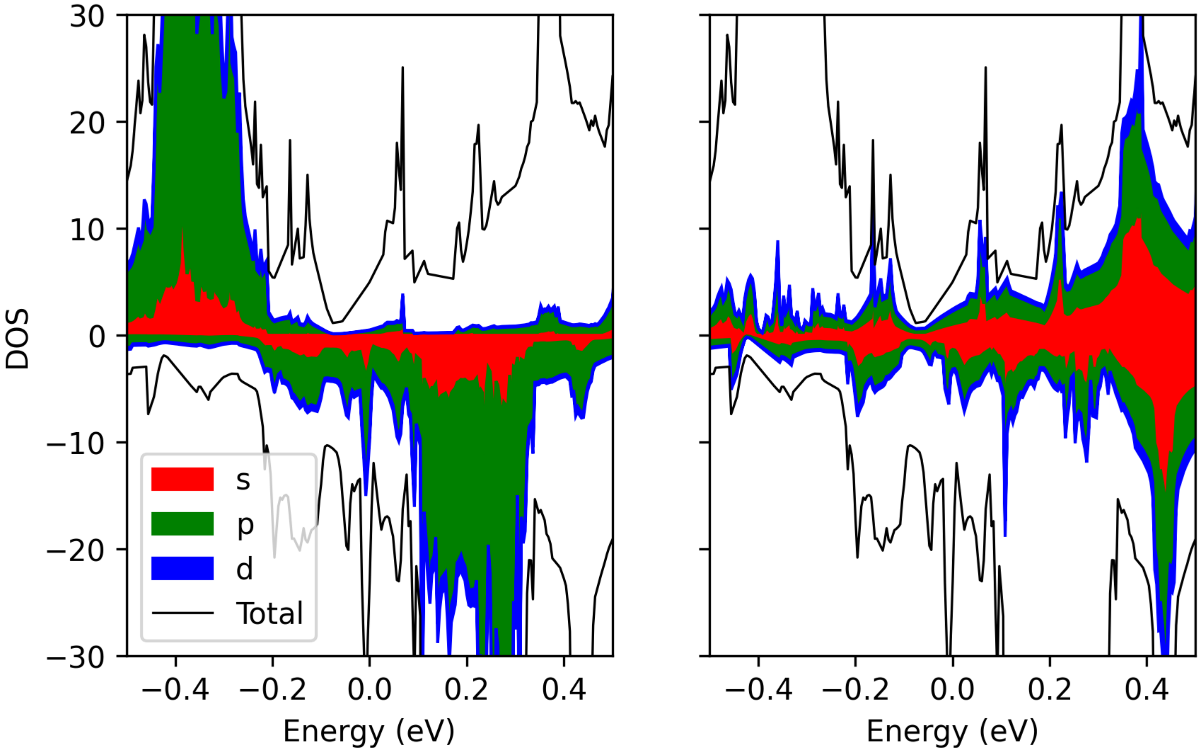

Figure 6.2 Projected DOS plots of the Te-passivated structure considering the bottommost AB layer of atoms (left) and the topmost (right). Special attention should be paid to features around –0.15 eV and 0.07 eV.

With the understanding that passivating only the nominally interior layer of the slab still allows for the formation of surface traps, we then moved to passivate the Hg-facing layer. Despite the increase in modeled electrons in the Hg pseudopotential, the same Z=1.5 pseudohydrogens were used. This configuration maintained the tetrahedral bonding structure while also, as demonstrated below, providing effective passivation of the surface states. This can also be demonstrated in the projected DOS plots: in the projections 1 and 4, there is no noticeable increase in the up-spin states around the Fermi energy when using the fully passivated structure as opposed to the Te-passivated one. This confirms the elimination of the surface states and is demonstrated in Figures 6.3 and 6.4. However, the original motivation for this passivation was to observe a positive band gap. As demonstrated in Figure 6.4, the up-spin states show a sizeable discontinuity between filled and unfilled states, spanning around 0.25 eV. This is nullified by the down-spin states that extend far from the conduction band and into the valence band, which is the origin of the "negative" band gap reported for HgTe previously.

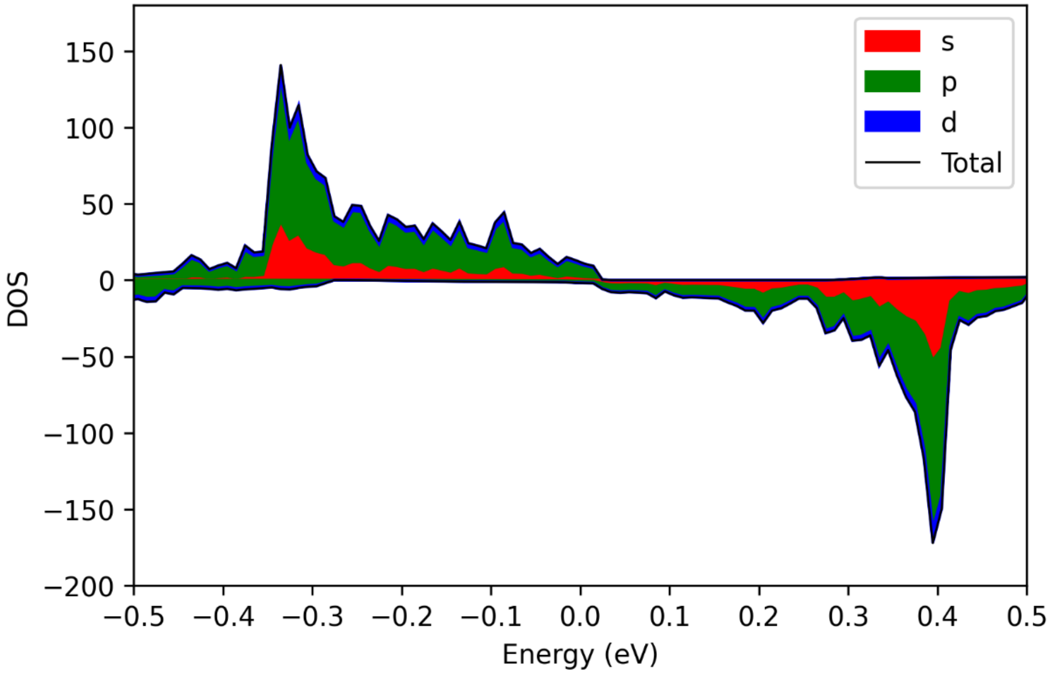

Figure 6.3 Density of states of the fully passivated 4 AB layered structure.

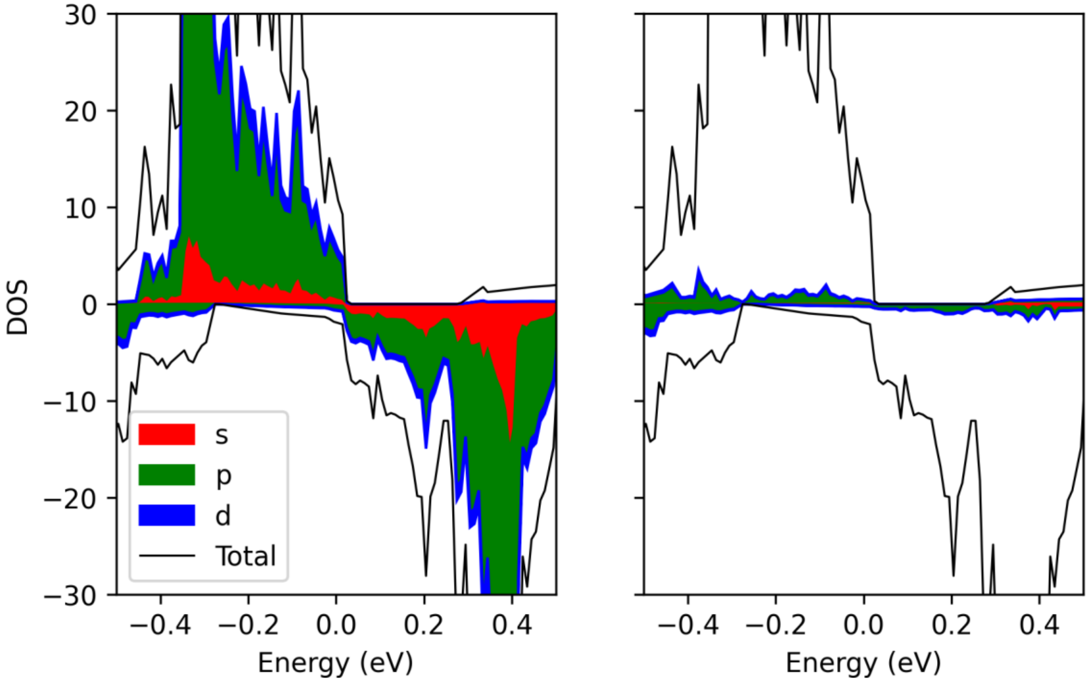

Figure 6.4 Projected DOS for the fully passivated structure considering the bottommost AB layer (left) and topmost AB layer (right). Notably, there are no significant increases in the up-spin states between the two projections.

The Fermi energy also considerably changes between the two structures. The Te-passivated structure has a Fermi energy of –1.4537 eV, while the fully passivated structure shifted down by approximately 1 eV with a Fermi energy of –2.4881 eV. This downward shift has two main causes. The Fermi energy as determined by VASP is the highest energy of the occupied eigenstates, or the top of the valence band in semiconductors. For the Te-passivated system then that has occupied surface trap sites above the presumptive valence band maximum around –0.2 eV in Figure 6.1, this would skew the Fermi energy upwards. Furthermore, with the introduction of hydrogen near the surface of the HgTe, the formation of bonds results in a net withdrawal of charge from the surface. Without any other strong dipole effects (see Chapter VII), this decrease in charge density directly relates to the decrease in the Fermi energy when passivating the structure. The overall band energies of the Te-passivated and fully passivated structures were –63.5752 eV and –74.8127 eV, respectively. Even when considering the added chemical potential of the added pseudohydrogens, the Hg passivation still results in a net reduction of 6.7443 eV compared to the unpassivated Hg surface. This large energy decrease does include effects due to the reconfiguration of Hg on the surface, but otherwise suggests that exposed Hg will readily react to eliminate any dangling bonds.

VI.2 Band Diagrams and Reduction of Layer Count

Lacking a discernible band gap in the fully passivated system, we then sought to increase the quantum confinement of the simulated structure. Decreasing the number of layers included in the slab further constrains a theoretical exciton and increases its energy. This increase in quasiparticle energy manifests as an increase in the energetic separation of the unoccupied and occupied states. The system was allowed to remain passivated due to the reduction of surface states indicated by the previous section. Overall, structures with 1-4 layers were simulated, and the DOS for each is given in Figure 6.5.

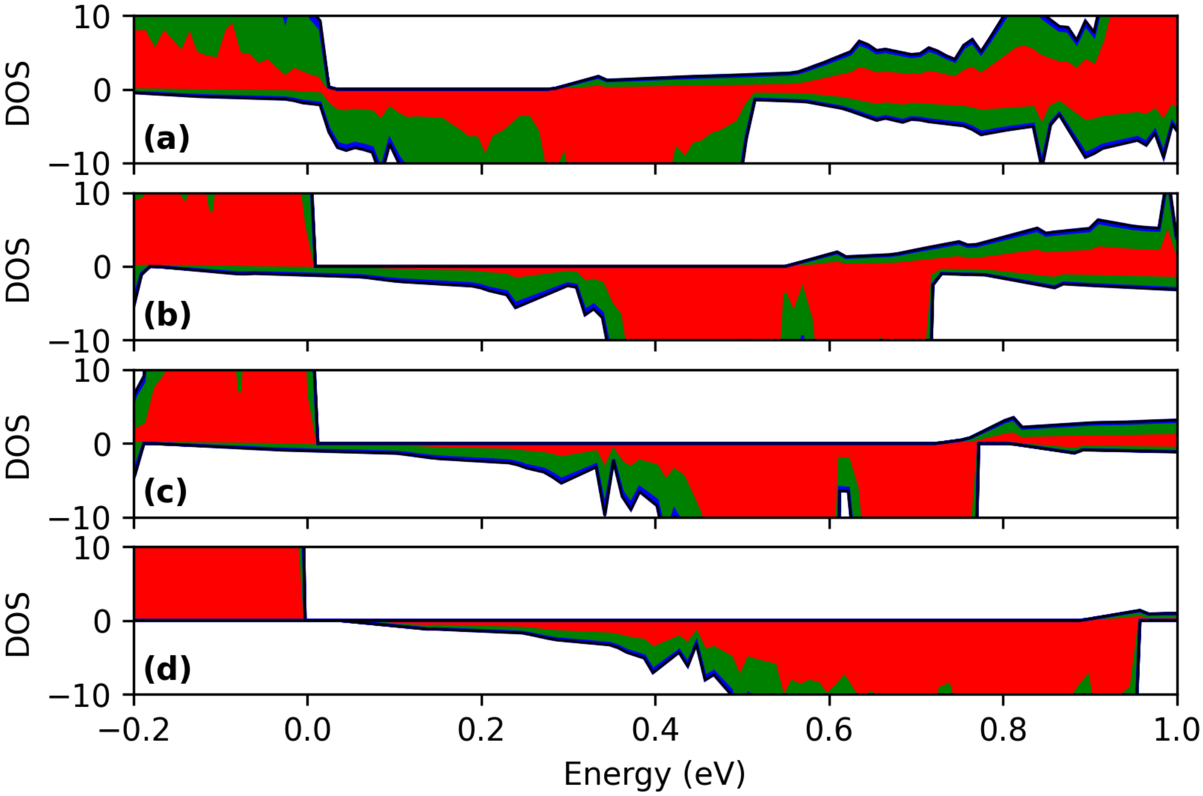

Figure 6.5 DOS plots comparing structures made with (a) 4, (b) 3, (c) 2, and (d) 1 AB layer of atoms.

The plots in Figure 6.5 reveal a few general trends. For instance, we notice that the gap between the up-spin dominated valence band and the corresponding down-spin conduction band broadens as expected when decreasing the layer count. If the down-spin states were to be neglected, this would emulate a reasonable band gap for this system. However, while the down spin dominated conduction band does indeed shift upwards in energy with decreasing layer count, it is not at the same amount, nor does it reveal a band gap until reaching the monolayer phase. The conduction band edge shows a very large increase in energy when going from 4 to 3 layers, but the shifts are relatively small thereafter. This behavior could be explained by acknowledging that the 4-layered structure is the only one in this series that has AB layers that do not interact with both surfaces: the middle two layers can interact with each other in a manner similar to that of the bulk material. This interaction could result in semi-metallic character similar to bulk HgTe. The structures with n>1 layers also have a non-zero number of states in the up-spin valence band above the Fermi level. This effect is not seen in the monolayer structure, so while large HgTe clusters that approach the bulk phase that see a vanishing band gap may see these states, it is unlikely that when the conduction and valence bands are well isolated in a quantum dot that this effective p-type character would manifest. The monolayer structure predicts that a pristine, well passivated quantum dot would instead behave intrinsically (however, this is complicated by observations made in Chapter V).

In Chapter IV we noted that the conduction and valence band DOS had a large contribution from *p*-orbitals in the tellurium projection. This can also be confirmed with band diagrams and atomic orbital projections. Figure 6.6 includes band diagrams for the 3-layered and the monolayer structures, which are colored by the fractional contribution of tellurium orbitals. The dashed lines represent down-spin bands. Most prominent of these is the band that descends from the conduction band and, in the case of the 3-layered system, crosses into the valence band around the gamma point. The dotted lines in this plot represent the Fermi energy as calculated during the band diagram calculation. This calculation is anomalous since it relies on a k-point path, rather than a mesh, and still employs Gaussian smearing rather than the tetrahedral method, leading to some anomalously high occupations. The band diagrams given here are corrected, with 0 eV representing the tetrahedral method obtained Fermi energy. While Figure 6.6 does confirm that the largest contribution to the states around the Fermi energy are from tellurium orbitals, we can also observe a trend hinted at by Figure 6.5. With decreasing layer counts, the relative share of the *p*-orbitals in the projected DOS plots also decreases. In Figure 6.6 this manifests as a decrease in the relative contribution of the tellurium orbitals. Instead, the states in the conduction and valence band are more heavily reliant on hydrogen orbitals, and the interloping band from the valence band is roughly equally contributed to by mercury and hydrogen orbitals. While this could simply be a representation of the relative amounts of HgTe and passivating molecules, it nonetheless emphasizes the need for an investigation into how other ligands can affect band alignment (see Chapter VII).

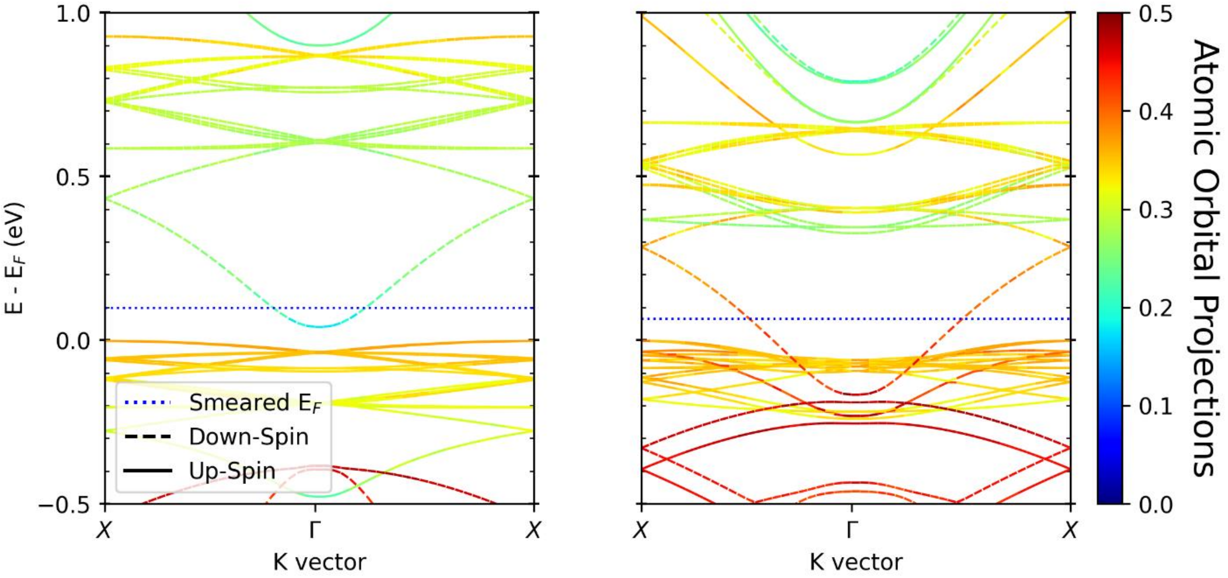

Figure 6.6 Band diagrams for a monolayer (left) and a 3-layered (right) structure. The bands are colored by relative tellurium orbital contribution.

VI.3 Development of the Mercury Vacancy Structure

The previous sections detail the electronic structure of a pristine HgTe (111) surface. Passivation allows for the removal of dangling bonds that manifest as states around the Fermi energy, and a reduction of layer count produces noticeable quantum confinement effects. This system should serve as a suitable model for a HgTe quantum dot, since the relative shifts in the bands and the development of the band gap in a monolayer regime is directly analogous to the reduction in edge size of the quantum dots. Moving forward then, the passivated 3-layered structure will be used. This reduces the computational load and any potential bulk-like interactions from the 4-layered model as noted in Figure 6.5 while still providing two subsurface layers for relaxations due to defects and substitutions on the top surface. Our primary subject will be a mercury vacancy on the Hg-facing surface of the slab. Previous studies on other transition metal chalcogenides suggest that the removal of the metal species will bring about mid-gap traps [38] The substitution of surface mercury atoms with other metals in Chapter VII also makes the mercury vacancy structure valuable.

The starting structure used during the ionic relaxation was the fully relaxed 3-layered passivated structure with one mercury atom and the corresponding passivating hydrogen removed. The initial ionic relaxation did not converge, even after five successive 24 hour runs. In retrospect, this is due to excessive unbounded line searches in the conjugant gradient minimization scheme. In scenarios when the energy landscape across the searched direction is relatively flat, it is sometimes possible for the interpolated energy minimum to have the same or a slightly higher energy than the binding points. In this case, the algorithm extends the search area by taking another trial point further along in the search direction. This can be repeated, pushing the atom further away from its starting position until a new energy minimum is detected. During the simulation, this new minimum was outside of the energy convergence criterion, allowing the run to continue indefinitely. The final obtained structure is provided in Figure 6.7. While ideally this extended search function allows for the conjugate gradient algorithm to locate minima far from the starting positions, the large distortion throughout the structure and near homogenization of the bottom layer is likely an overcorrection.

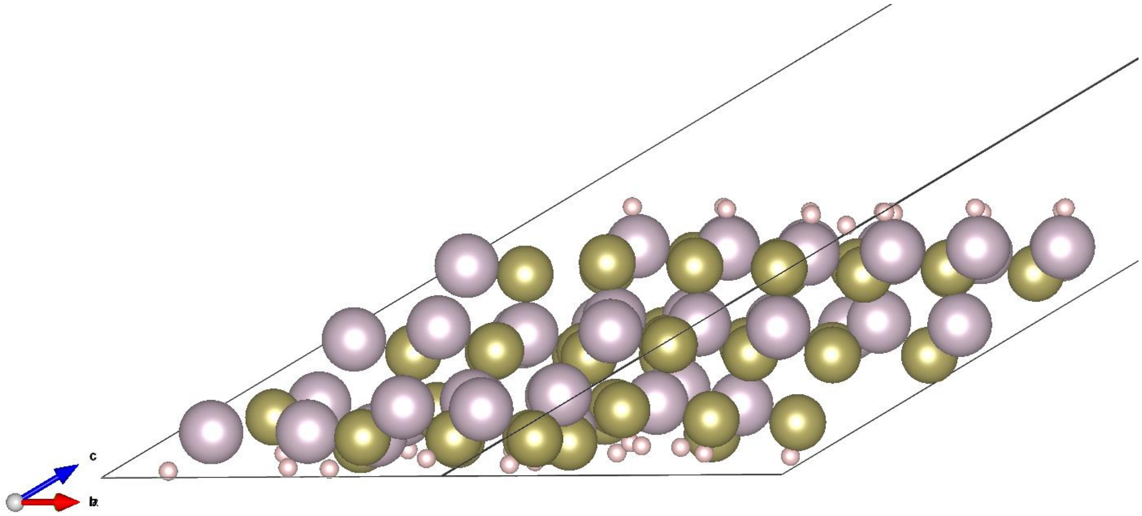

Figure 6.7 Profile of the initial simulated structure, with 3 layers and a surface mercury defect, after 5 successive runs.

With this deep distortion and fragility in mind, the structure was relaxed in a more cautious manner. “Selective Dynamics” was enabled in the initial POSCAR file, which allows the specification of which lattice vectors a given atom is allowed to move along. Since the greatest amount of distortion was witnessed in the bottom layer of the structure, the top two layers were allowed to freely relax, while the bottom was fixed. This step converged quickly but, as noticeable in Figure 6.7 as well, a hydrogen at the top of the structure was displaced, and now lies within the defect itself. The reduction of the angle between the subsurface tellurium layer and the newly unpassivated mercury atom indicates that it has undergone a similar surface relaxation to those previously covered and could introduce surface states into the electronic structure. Two branches were allowed to proceed: in the first, the hydrogen was reset to an appropriate distance above the newly relaxed mercury while keeping the original constraints in place (ReH). In the second the hydrogen misplacement was ignored, and the bottom tellurium-facing layer was allowed to relax while the rest of the structure was frozen (Te-relax).

Both the ReH and Te-relax trials converged. The constraints were then removed on the ReH structure, but again, the structure destabilized due to unbounded line searches. This was also the case when just allowing the bottom layer to relax, like in the Te-relax trial. The Te-relax trial, however, did converge with the constraints removed. The unpassivated mercury however was still a concern. The unpassivated mercury and the hydrogen atom that fell into the defect were fully reset to be in line with the other surface atoms. This pair of atoms was then allowed to relax with the rest of the structure constrained. Once again, the top two AB layers of atoms were allowed to relax with the bottom Te-facing layer constrained. This structure is arguably similar to the starting structure, with the possibility of the bottom layer destabilizing with unbounded line searches. Instead, a quasi-Newton algorithm explored at the end of Chapter AA was used, with all the atoms allowed to relax. Up until this point, the criterion for convergence was based on a converging energy between trial steps of the conjugate gradient algorithm. Instead, when using the quasi-Newton algorithm, we elected to use a force-based convergence criterion: the magnitude of the force on each atom must be less than 0.03 eV/A. This criterion is more suitable for the quasi-Newton algorithm that does not consider the total energy of the system. This process yielded the well converged structure in Figure 6.8.

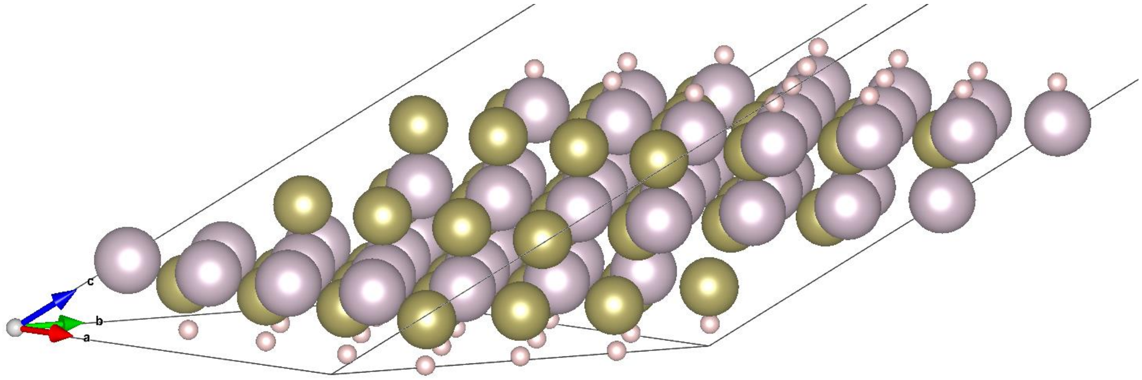

Figure 6.8 The final, fully relaxed 3-layered structure with a surface mercury vacancy.

The final structure in Figure 6.8 shows some reasonable differences compared to its stoichiometric counterpart. On the Hg-facing surface itself, the passivating hydrogens on the six mercury atoms nearest to the vacancy site have bent away from the site, indicating a lack of electrons in the region. Similarly, in the second layer, mercury atoms beneath the site have been pulled towards the tellurium subsurface layer. This effect can also be seen in the third layer, where the tellurium atom directly beneath the site has been pulled upwards, and its passivating hydrogen has become more tightly bound. Having calculated the total energy of the defect-free structure and the chemical potentials of bulk Hg and gaseous H_2, we can determine the formation energy of this defect to be 1.3757 eV. We should acknowledge that this is an upper bound for the true formation energy since the chemical potentials were taken to be the unit total energy of Hg/H_2 in the simulated supercell, which themselves are an upper bound to the true chemical potentials [39].

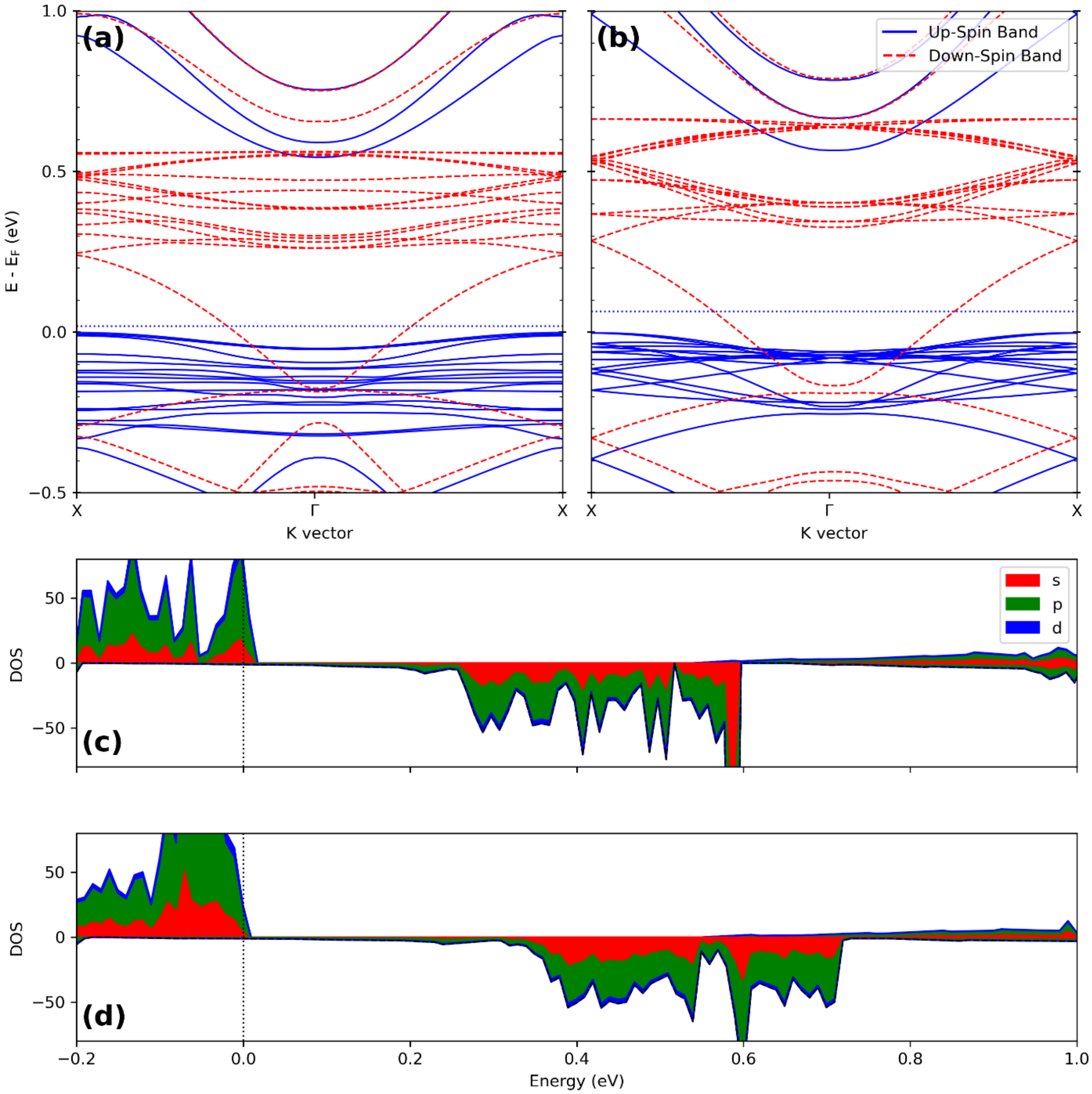

Figure 6.9 Band diagrams and DOS plots for both the pristine (b, d) and mercury vacancy (a, c) structures.

The band diagram and DOS plots of the defective structure in Figure 6.9 reveal that the HgTe surface appears to be somewhat defect tolerant. In the band diagram we notice an appreciable separation of bands in the valence band when compared against the pristine structure. This splitting manifests as a substantial increase in the number of states available just above the Fermi level. As noted above, the Fermi level in VASP is chosen by the energy of the highest occupied orbital. Both the pristine and the defective structure have very similar Fermi levels: –3.0794 eV and –3.0673 eV respectively. This does not distinguish between the true top of the valence band that we would expect in the pristine system and the possible filled vacancy states near the top of the valence band, which would explain the minor but noticeable contraction of the conduction band towards the Fermi level. While single, neutral mercury vacancies appear to be shallow trap states, these could be more problematic in LWIR applications, where these trap states would appear closer to the midgap. For applications approaching NIR however, these available states would likely act as acceptor states, leading to more p-type character in a nanocrystal system.

Previous DFT studies of metal vacancies in other II-VI colloidal quantum dot systems have suggested that the removal of metal vacancies, which result in a 2-coordinated chalcogen center induce midgap trap states [34]. These trap states are highly localized and attributable to the 2-coordination chalcogen center. The model simulated by Houtepen et al. Included three unique faces of CdSe in a nanocluster, which allowed the 2-coordinated Se center to appear with a Cd vacancy. This model suggests that tetrahedral {111} HgTe CQDs, with uniform faces, edges, and surface stoichiometry would be uniquely defect tolerant compared to spherical nanoclusters, since a minimum of two metal vacancies must form adjacent to the same Te site for the 2-coordinated Te center to manifest.

Chapter VII. Ligand and Surface Atom Substitutions

The neutral mercury vacancy in the 3-layered (111) HgTe model produced defect states that would lead to unintentional p-type doping or charging effects under electric fields. The trap states also have the potential to contribute to recombinative losses in optoelectronic devices, especially in the LWIR regime. Having a higher degree of control over the conduction type of HgTe quantum dot films is imperative for improved device performance. Presently, reports of p-type doping through the use of an Ag_2Te CQD film and a cation exchange reaction have already demonstrated competitive performance [1]. This is attributed to the accumulation of silver species on the surface of otherwise pure HgTe colloidal quantum dots. DFT should be able to provide an *ab initio* confirmation of this mechanism. Furthermore, potentially in part because of single mercury vacancies, a single substitutional model for inducing n-type doping within HgTe CQD films has not been demonstrated. Previous reports that induce n-type doping demonstrate the shift of the Fermi level towards the conduction band with reduction of dot size [12], but the effect is small and, in devices, disallows precise wavelength tuning due to the reliance on dot size.

Here, heteroatoms are explored as a universal method of tuning the Fermi level position for n-type doping. Ligands also have the potential to have an outsized impact on device performance by manipulating the alignment of the conduction/valence band edge positions, as discussed in Chapter I. While a full qualitative study cannot be presented, as noted in Chapter V, here, relative shifts in the Fermi level due to various ligands involved in HgTe CQD processing is presented. It should be noted that throughout this chapter, we will frequently compare energies of different structures to evaluate the thermodynamic stability of reaction/doping pathways. For the sake of clarity, all calculations will take the form of equation (1) below:

$$E_{rxn} = E_f - E_i + \sum_i n_i \mu_i \tag{1}$$

Here E_{rxn} is the net energy change from going from the initial simulated structure E_i to the final simulated structure E_f. If the structures have dissimilar numbers of atoms of a given species, their chemical potentials μ will need to be taken into account (where $n > 0$ and $n < 0$ correspond to adding and removing atoms, respectively).The meaning of E_{rxn} will be context dependent; it is used in the context of adsorption (adsorption energy) and the occupation of Hg vacancy sites (formation energy). Regardless of context, a $E_{rnx} > 0$ should be understood to represent an endothermic, thermodynamically unfavorable pathway, with the opposite being true for $E_{rxn} < 0$.

VII.1 Silver Chloride

To investigate the mechanism for silver-induced p-type doping in HgTe CQDs, we explored two pathways. Cation exchange from Ag_2Te to HgTe quantum dots acts as the source of silver to the system. In one pathway, we model a system in which the cation exchange is incomplete, and AgCl remains chemically associated with the surface. This would be akin to substituting a Hg-H atomic pair at the surface with AgCl. In the second pathway, the cation exchange is complete and silver chloride species are entirely liberated. However, after subsequent drying of a CQD film, AgCl remains adsorbed to the highly coordinated FCC site on the Hg rich surface. A subtle difference between these two mechanisms is that the Ag substitution pathway should be highly localized to the original Ag_2Te application. While secondary ion mass spectrometry indicates the presence of silver throughout a HgTe film capped with cation exchanged Ag_2Te, the authors note that the ion beam could have pushed silver ions through the porous CQD layers [11]. Without an adequate understanding of the silver distribution through device layers, both mechanisms presented here are valid. The quasi-Newton algorithm with force-based convergence was used in the relaxation of these structures.

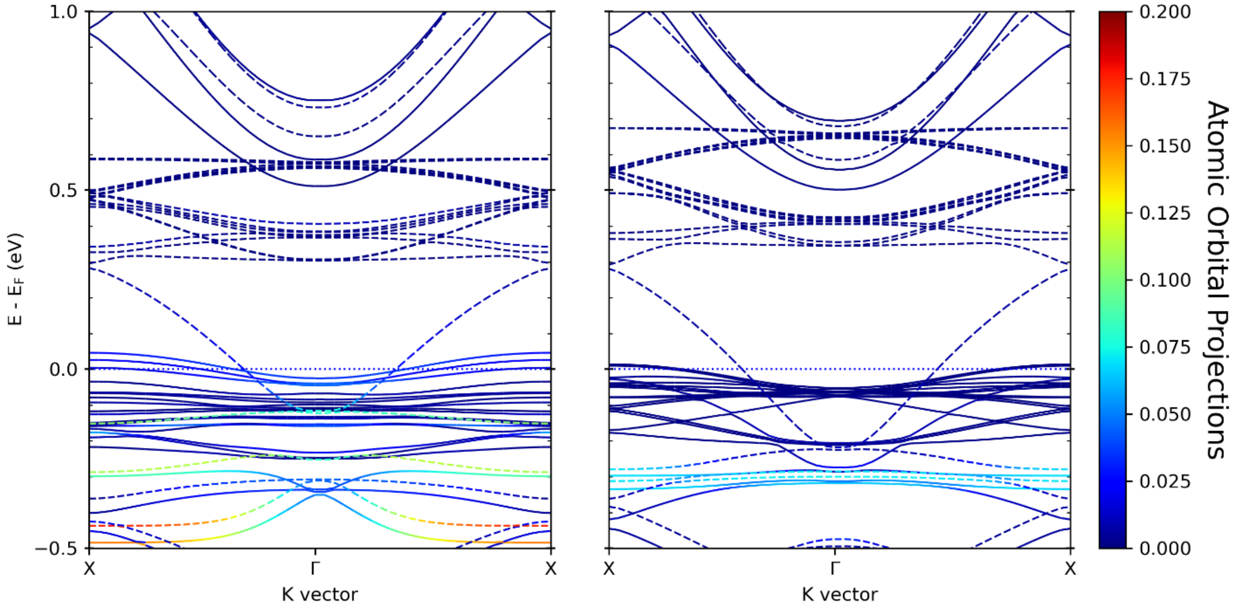

Figure 7.1 Band diagrams for the silver chloride in a substituted (left) and an adsorbed (right) configuration. The bands are colored by the atomic orbital projection of the added silver atom.

Presented in Figure 7.1 are the band diagrams of the substituted and adsorbed silver structures. Highlighted in the color bar is the atomic orbital projection for the silver atom. As demonstrated above, in both cases, bands that lie below the valence band are noticeable. These states should act as acceptor states and contribute holes to the system. As noted in Chapter V, many of the states near the Fermi level are surface states due to the Te-H interaction. That these surface bands are partially emptied serves to demonstrate the ability for the silver states to act as acceptors (although the contribution of filled states well below the Fermi level would also act as acceptors, even at 0 K). We should also acknowledge that regardless of the completeness of the cation exchange reaction, silver species will be liberated into the HgTe film, meaning that it is possible for both pathways for p-type doping to exist and contribute. The ability of adsorbed silver to induce p-type doping also suggests that devices with graded effective doping concentrations are possible if silver diffuses through underlying HgTe layers. This concentration difference in a band-like understanding of device physics would induce an electric field allowing for low voltage operation of photodiodes.

While both pathways induce bands near the valence band to contribute to p-type doping, thermodynamics suggests that the adsorbed silver pathway is heavily favored. The total energy of the silver substitution structure was –240.4513 eV, compared to the defect structure's –235.8164 eV. Taking the difference, and then considering the chemical potential of both the silver and the chlorine atoms, the formation energy of this substitution is 0.0269 eV. This would make the silver substitution model rather unstable, with the system preferring to exclude the silver from the topmost mercury layer. This might be expected when considering that the cation exchange preferentially swapped mercury in place of silver. The adsorbed model, by comparison, yields an adsorption energy of –0.3620 eV. This indicates that the FCC sites on the Hg-rich surface are suitable locations for the aggregation of silver ions, and this aggregation can influence p-type doping in HgTe CQDs. Assuming the complete conversion of Ag_2Te to HgTe, this could make for an extremely high doping density. The surface here assumes a silver density of about 10^{14} cm^{-2}, and there are 8 more identical sites in the simulated cell. We cannot assume a 1:1 silver adatom-to-charge ratio, but it is clear that the dopant density can be rather high.

VII.2 Indium Species

Indium as a group III element is a prime candidate for contributing electrons directly to the conduction band of HgTe through donor states. Indium in particular, with an atomic radius of 155 pm, was chosen because of its similar size to mercury (150 pm). Furthermore, indium salts like indium chloride could be introduced to a HgTe CQD film during solid state ligand exchange; indium chloride for instance is soluble in ethanol. Similar to the previous section, we assumed that indium species, in this case an indium atom passivated with pseudohydrogen, could contribute to the dispersion of a HgTe surface through substitution (and passivation of surface mercury vacancies), and adhesion to FCC sites. The substitution very quickly converged using the quasi-Newton algorithm and force-based convergence. The same was true for the adatom structure. Unlike in the silver chloride case however, the adatom delaminated from the surface, with or without the passivation of the nearest mercury atoms. This delamination and strong force near the surface stopped any further investigation into the adatom solution. While it is possible that indium may occupy other sites on the Hg surface, we found that it is much more likely to occupy Hg vacancies.

To model the passivation of surface Hg vacancies, we modeled the transition of a free indium atom separate from a defect to the indium occupying the vacancy site. Ideally, this might be performed with the nudged elastic band (NEB) method implemented in VASP or its derivatives. The NEB method relies on interpolations, or images, between the reactant and product structures to find the minimum energy path of the transition. The images are "connected" with elastic bands, and the forces due to these bands can be used to maintain the spatial separation of the images and prevent the images from sliding towards either local energy minimum. This allows for structural minimization along a transition pathway, approximating the minimum energy path. In preparation for an NEB calculation, well converged end points must be interpolated to form images. The end point of the calculation was the simple substitutional In-H structure made previously. Before the transition, the In-H molecule was placed directly over the vacancy site of the structure modeled in Chapter VI. A single self-consistent electronic minimization was performed to evaluate the forces on the molecule. The forces on the In-H system were well within our convergence criterion 0.6 nm from the vacancy site. Initially, 5 images were made between the two endpoints with a simple, linear interpolation (resulting in a spacing of approximately 0.1 nm).

A full NEB minimization was not completed; the computational cost of the procedure is very high and was not close to converging after the first 48 hours. Instead, we elected to use an approximation of the minimum energy path. Beginning with the endpoints and each of the images, a self-consistent electronic minimization was performed. This was done using the tetrahedral method as described in Section VI.1 with a fine *k*-point mesh to obtain the most accurate energy possible while still being comparable to other calculations made thus far. The highest energy was found when the InH molecule was 2 Å above the vacancy site. Four more images, from 2.35 Å to 1.65 Å were added, and their energies were calculated. The energies are plotted in Figure 7.2.

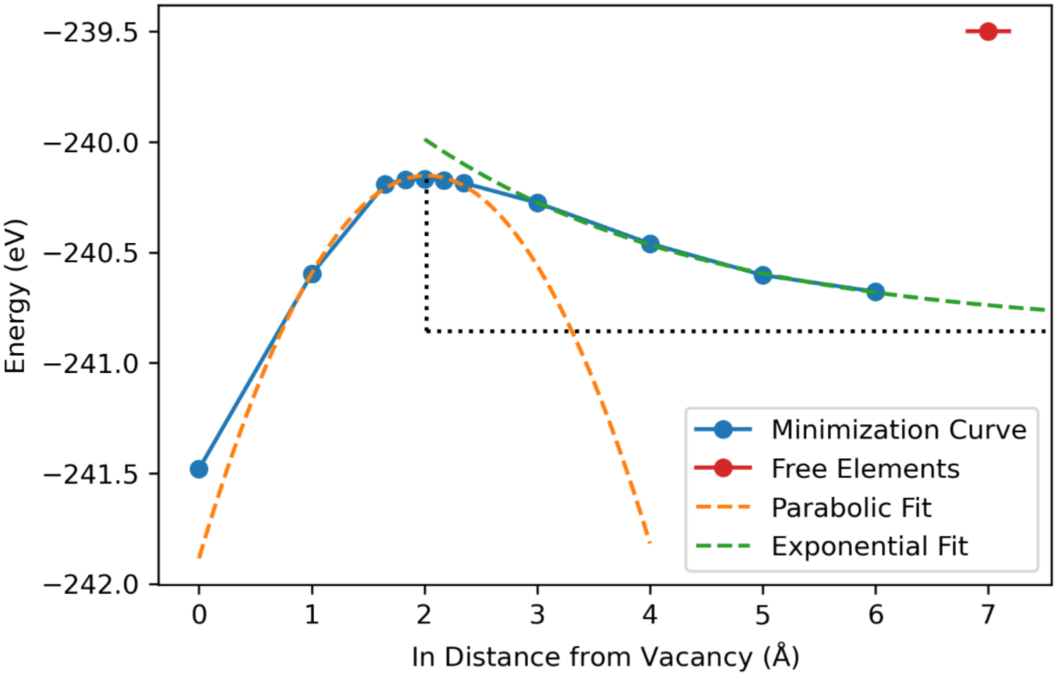

Figure 7.2 Estimation of the minimized energy path for an indium atom falling into a surface mercury vacancy.

An exponential fit was made for points further than 2.35 Å to estimate the energy of an infinitely separated InH molecule and slab. Likewise, a parabolic fit was made for points closer than 2.35 Å to identify the energy maximum. The energy approaches –240.9 eV at infinity, and reaches its maximum of –240.2 eV at an InH distance of 2.02 Å. This results in an activation energy of 0.7 eV, or about 67.5 kJ/mol. This result indicates that the reaction may proceed rather quickly, especially at elevated temperatures during CQD synthesis – the decomposition of peroxide for instance has an activation energy of around 75 kJ/mol [40]. In addition to the qualitative observation of the exothermic behavior of the reaction in Figure 7.2, the estimation of the formation energy is –1.9806 eV, when considering the chemical potentials of the added indium and hydrogen atoms. Plotted at 7 Å in Figure 7.2 is the combined total energy of the defective surface and the chemical potentials of indium and hydrogen. It is clear that the In-H interaction is very strong, leading to the drop in energy towards –240.9 eV observed when simulating the InH molecule. This suggests that the activation energy and formation energy presented here would likely be modified by the specific indium species used in the reaction.

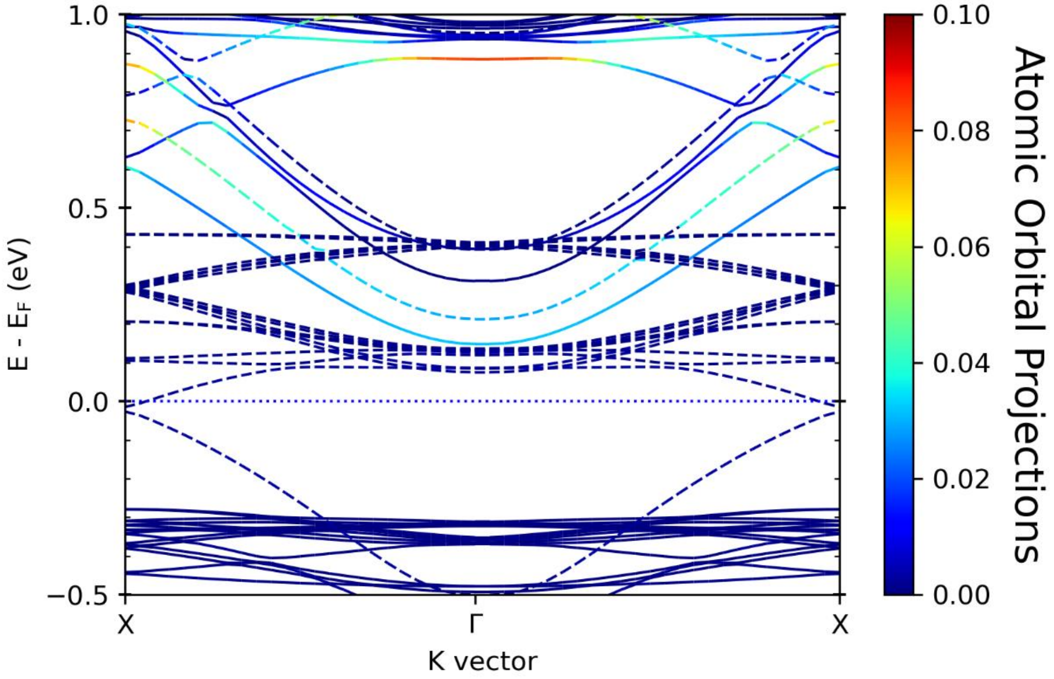

Figure 7.3 Band diagram for a HgTe surface with an indium substitution. The bands are colored by the atomic orbital projection of the indium atom.

The band diagram of the indium substitution reveals the appearance of bands above the conduction band minimum. As noted in Chapter V, this should be the down-spin state that dips below the relatively flat surface state bands near the bottom of Figure 7.3. The Fermi level in this structure is near the top of the first conduction band dispersion, indicating that the inclusion of indium on the surface has successfully donated electrons to the system. This would manifest as n-type character in a CQD film. Ideally, as mentioned above, indium could easily be incorporated into the CQD film during ligand exchange steps where it could serve to occupy mercury vacancies. This would lead to a stronger correction of the electrochemical potential compared to a simple indium exchange if mercury vacancies prove to impart p-type behavior. Another possible route not explored here is the homogeneous incorporation of indium into the nanocrystals during synthesis, which may offer a higher degree of control over the active doping level.

VII.3 Ligand Surface Modifications

In CQD photodiodes the fast extraction of charge from the CQD film and into electron/hole transport layers is vital for high efficiencies. This makes the relative position of the conduction and valence bands extremely important to the performance of devices. The use of different passivating ligands in lead-based quantum dots has been shown to greatly modify the conduction/valence band edges, as well as the electrochemical potential [9]. A large variety of ligands are used in the hot-injection synthesis of HgTe colloidal quantum dot films, but these effects have not been theoretically explored. Here, the base 3-layer structure is again modified to simulate a quantum dot surface with ligand modifications. As noted in Chapter V, the presence of surface states makes the true position of the Fermi level and conduction/valence band edges difficult, but we expect that the relative shift in the Fermi level would be informative, allowing for an approximate determination of the conduction/valence band edge shifts.

For this study, four different ligands were used: chlorine, ethanedithiol (EDT), ethyl mercaptan (EM), and acetic acid (AA). At first, a single pseudohydrogen on the Hg-facing surface was substituted. In the case of AA, it has been generally found that it is more thermodynamically favorable for both oxygens of the carboxyl group to be bound to the metal surface, so two pseudohydrogens were substituted in that case [41]. Initially, the structures generated with the 3-layered structure used the same 2x2 supercell detailed in Chapter IV. The structures proved to be difficult to converge with force-based convergence with the quasi-Newton method. For instance, one of the first ligands attempted was AA, which took over 230 ionic steps to fully converge. To increase our throughput, we opted to use energy-based convergence with the conjugate gradients (CG) algorithm. We ultimately found that this ligand density (about 1/16th of all available sites) produced a very small shift in the Fermi level –

around 0.12 eV. It is important to note however that the use of an energy-based convergence criterion with the CG algorithm meant that the converged structure is very sensitive to our starting conditions and parameters and could allow for different conformations to exist with lower forces and total energies. So, while a small shift is possible for these ligand densities, we sought to elevate the effect well beyond any possible computational inconsistencies.

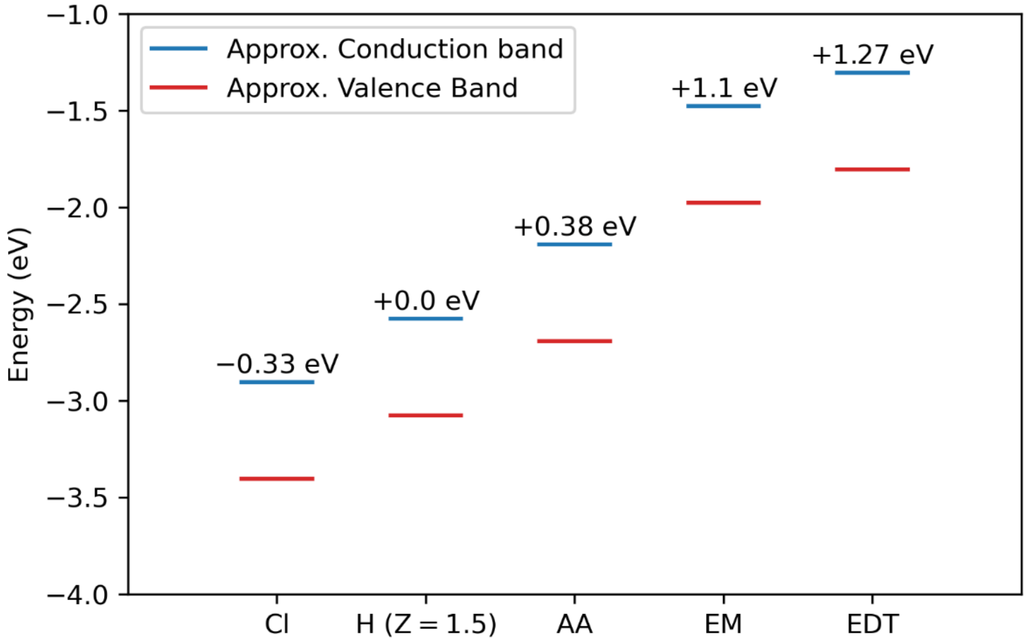

Figure 7.4 Relative shifts of the Fermi level with different ligands compared to the nominally pseudohydrogen passivated slab. The conduction and valence band positions are illustrative only.

To augment the Fermi level shifting effect, we elected to substitute all possible ligand sites on the surface. For AA, this meant 8 total molecules were present, and 16 for all others. Adding in some cases hundreds of atoms to the system was deemed too impractical, so the lattice vectors **a** and **b** were halved in magnitude, making a 1x1 supercell and leaving 4 sites (2 for AA). This greatly reduced the computational cost of the calculations, and for simple Fermi level calculations in neutral systems, relying more heavily on the periodic boundary conditions should not sacrifice much accuracy. The Fermi level shifts, relative to the structure passivated with hydrogen, are shown in Figure 7.4. Collectively, the ligands span a 1.6 eV range. The Fermi level shift is tightly correlated by the induced surface dipole and the dipole of the ligand itself. Chlorine ligands for instance yield a slab with the highest work function: the strong ionic behavior of the Cl-H bond induces an electric potential near the surface of the slab, causing a downward shift in the conduction and valence bands. Likewise, while we note that the thiol-based ligands show a similar upward shift in the Fermi level compared to pseudohydrogen (likely owing to sulfurs large size and low electronegativity) this shift is smaller for EM than EDT. The thiol group at the end of EDT is likely partially compensating for and screening the overall dipole experienced by the slab's surface. We should expect that these screening effects would be more complicated in solid films, where ligands can become interdigitated between individual nanocrystals.

Overall, the shifts demonstrated here align well with a surface dipole understanding of ligands. While many ligand exchange techniques form aggregated films using EDT, we have demonstrated here that a wealth of other small organic materials could potentially be used to induce shifts in the conduction/valence band edge positions. Acetic acid for instance demonstrated a downward shift of up to 0.89 eV. While contacts for HgTe CQD materials are often made from silver and gold materials, a downward shift in the conduction band could make lower work function alternatives like Al available to ohmic contact. This study is however limited by the surface states discussed in Chapter V. A more complete review would ideally be able to identify the conduction/valence band edge positions relative to the Fermi level explicitly. Furthermore, the survey of ligands here is incomplete, as amines are also often used in HgTe CQD fabrication. Care should also be taken to examine interdigitation screening effects, and it is unlikely that a 100% ligand exchange would be achieved; hybrid systems could also be investigated.

Chapter VIII. Conclusions and Future Work

Overall, the work performed here represents a considerable contribution to the theoretical understanding of mercury telluride CQDs, especially those with {111} tetrahedral faces. Herein, we presented some of the first calculations of the surface energy of the (111) surface in HgTe and demonstrated the validity of a relatively new method [32]. We argued that the successes of this method could be explained by the similar electronegativities of mercury and tellurium, and that the overall slab's surface energy was dominated by the mercury rich face. This trend is clearly based on the deformation of the mercury rich surface, as shown in Figure 4.4. Furthermore, we determined the formation energy of several defects and substitutions to the mercury rich surface, which led to a theoretical understanding of both p-type and n-type doping using heteroatoms in HgTe CQDs, and presented qualitative insights to ligands frequently used in HgTe nanocrystal fabrication. In particular, the doping mechanisms we identified offer some key potential improvements to the state of the art in HgTe CQD technology.

We would first like to highlight the identification of the theoretically preferred mechanism of p-type doping in cation exchanged Ag_2Te. Through a DFT study, we have shown that while substituting Ag for Hg on the mercury rich surface was unstable, silver readily adsorbed to FCC sites on the surface. This is significant since it suggests that the local p-type doping sought through a sacrificial Ag_2Te layer may be lost; instead, the diffusion of silver ions can lead to various distributions of p-type behavior, since adsorbed silver can act as an active dopant. Interestingly, the use of free silver ions in a solution of silver nitrate was shown to destroy photodiode characteristics in HgTe photodiodes, likely attributable to the rapid diffusion of a solution with a high dopant potential [11]. Overall, limiting the diffusion of silver species will be imperative for the local doping of HgTe nanocrystals, which naturally invites further investigation. Moving from this introductory study, one may be interested in evaluating the stability of silver in an ionic form aggregating on the surface, instead of immediately forming AgCl. Also of interest would be the movement of silver species themselves across the HgTe surface, made possible through molecular dynamics or transition state DFT, and the stability of different sites than the one studied here. An in-depth study of the diffusion dynamics may also necessitate thermal effects which are not considered in the ground state 0 K DFT calculations performed here.

We also demonstrated the capacity of indium species to readily occupy mercury vacancy sites and induce n-type doping, which offers a significant opportunity for device fabrication with HgTe CQDs. N-type doping is most often achieved through modification of syntheses that prohibit well behaved homojunctions with uniform optical properties through a device, so a potential avenue for a universal doping method is deserving of further study. Not considered here for instance is the possibility of a mercury exchange process in which indium favorably substitutes mercury on the surface of the CQD. This could be investigated thermodynamically, as well as with transition state DFT. An indication that indium species will readily undergo cation exchange with mercury would suggest that rapid quenching of the reaction or a very well controlled amount of indium should be implemented when introducing indium after the CQD synthesis. As another pathway, subsurface indium should also be investigated for stability and n-type character. If proven viable, this could allow for the direct incorporation of a small amount of indium into the CQD during synthesis, where both indium and mercury precursors are present during hot injection. This method also has the advantage of being highly tunable and localized, since subsurface indium would be unlikely to diffuse into neighboring layers.

Also relevant to n-type doping were our investigations of the Te-H interactions in Chapter V. We would like to highlight that the correctly passivated three-layer structure with an ideal 1:1 Hg:Te ratio did readily display n-type character (see Figure 5.2), which can then be made increasingly p-type with the addition of a mercury layer below the bottommost tellurium facing layer. This behavior is generally opposite to what's observed experimentally, where excess mercury can result in n-type behavior [12]. This effect should be explored further to confirm its origins, but it is possible that a global dipole exists across the slab in the 1:1 Hg:Te configuration that is corrected with the addition of the bottom mercury layer. The manifestation of n-type doping with excess mercury could also be explored theoretically through the modelling of mercury containing ligands and adatoms. Important to this study would be the development alternative HgTe faces, since nanocrystals synthesized with n-type doping are typically more spherical in shape due to the use of a different tellurium precursor [12].

The obvious limitation of the work presented here was the presence of spin-splitting and surface states due to the Te-H interaction discussed in Chapter V. As discussed in that chapter, none of the qualitative observations made here should be impacted through the correction of the passivation, but for the sake of clarity and thoroughness our calculations should be repeated with the new passivation scheme. This would also allow us to clarify a few points and expand on our present work. For instance, the vacancy models developed here focus on neutral mercury vacancies, which appear to show little impact on the states closest to the Fermi level, and could instead introduce acceptor-like states in the valence band. This small p-type effect was noticeable in the DOS plots for the vacancy structure and could contribute to an innate p-type doping in hot-injection synthesized CQDs. An observable band gap obtained with DFT+U and the lack of spin-splitting and Te-H states would allow for this to be proved definitively. Building on this, if the

{111} tetrahedral HgTe CQDs prove to be somewhat electrically tolerant of single neutral mercury vacancies as our study suggests, two or more vacancies could be introduced. The model for traps in CdSe suggests that having 2-coordinated chalcogen sites leads to midgap states in II-VI semiconductors, which could be modeled here through neighboring pairs of mercury vacancies.

The development of a clear, observable band gap also enables studies of different changes to the (111) surface. For instance, the tellurium vacancy was introduced in Chapter V and no conclusions were drawn about its character. A clear band gap would allow us to determine if {111} tetrahedral CQDs are tolerant to both kinds of single vacancies. When using the slow-reacting TOPTe tellurium precursor, it's possible that these tellurium vacancies would be more common, due to the rapid reaction of mercury species which prevents access to underlying tellurium sites. Building on this β-HgS, which has a zincblende crystal structure similar structure to HgTe has been shown to exhibit semiconductor behavior with a positive band gap [42]. Introducing Te-vacancies would invite studies into substitutions, like with sulfur atoms to create alloyed HgTeS CQDs. The effect of sulfur substitutions could be similar to that of HgCdTe and result in the growth of the band gap with no change in the overall dot size. This in turn could enable films with a large shift in conduction band energy, while maintaining a consistent valence band energy, like an ideal hole transport layer.

The use of a clear band gap would also allow us to explore the effects that the various ligands presented here have on the DOS and band diagrams, rather than the position of the Fermi level alone. While we were still able to demonstrate the clear dipole-dependent shift of the Fermi level, this would clarify any potential doping pathways presented by the alternative ligands. We should also stress that the ligands used in this work are very well suited to the final ligand exchange step to reduce interdot distance and improve conductivity. The ligands we selected were purposefully small to minimize the computational load but were still able to demonstrate large changes in the Fermi level position. This could allow for solid films with decent conductivity that interact with one another to form heterojunctions, or are used to form ohmic contacts with metals with previously inaccessible work functions like aluminum. Of note however is that the ligand studies we performed here are not complete. For instance, oleylamine frequently used in HgTe CQD synthesis does not have a good analog in our simulations. Furthermore, it is highly unlikely that when undergoing a ligand exchange process the nanocrystal completely exchanges ligands from one species to another. The effects of hybrid ligands, especially if any are shown to contribute dopant-like behavior, should be explored.

References

[1] M. M. Ackerman, M. Chen, and P. Guyot-Sionnest, “HgTe colloidal quantum dot photodiodes for extended short-wave infrared detection,” *Applied Physics Letters*, vol. 116, no. 8, p. 083502, Feb. 2020, doi: 10.1063/1.5143252.

[2] G. Kresse and D. Joubert, “From ultrasoft pseudopotentials to the projector augmented-wave method,” *Phys. Rev. B*, vol. 59, no. 3, pp. 1758–1775, Jan. 1999, doi: 10.1103/PhysRevB.59.1758.

[3] C. Kittel, *Introduction to Solid State Physics*, 8th ed. John Wiley & Sons Inc., 2005.

[4] D. H. McIntyre, C. A. Manogue, and J. Tate, *Quantum Mechanics: A Paradigms Approach*. Pearson, 2012.

[5] D. Thureja *et al.*, “Electrically tunable quantum confinement of neutral excitons,” *Nature*, vol. 606, no. 7913, pp. 298–304, Jun. 2022, doi: 10.1038/s41586-022-04634-z.

[6] P. Sheykholeslami-Nasab, M. Davoudi-Darareh, and M. H. Yousefi, “Modeling and numerical simulation of electrical and optical characteristics of a quantum dot light-emitting diode based on the hopping mobility model: Influence of quantum dot concentration,” *Chinese Phys. B*, vol. 31, no. 6, p. 068504, Jun. 2022, doi: 10.1088/1674-1056/ac364b.

[7] C. Gréboval *et al.*, “HgTe Nanocrystal-Based Photodiode for Extended Short-Wave Infrared Sensing with Optimized Electron Extraction and Injection,” *ACS Appl. Nano Mater.*, vol. 5, no. 6, pp. 8602–8611, Jun. 2022, doi: 10.1021/acsanm.2c02103.

[8] P. R. Brown *et al.*, “Energy Level Modification in Lead Sulfide Quantum Dot Thin Films through Ligand Exchange,” *ACS Nano*, vol. 8, no. 6, pp. 5863–5872, Jun. 2014, doi: 10.1021/nn500897c.

[9] D. M. Kroupa *et al.*, “Tuning colloidal quantum dot band edge positions through solution-phase surface chemistry modification,” *Nat Commun*, vol. 8, no. 1, p. 15257, May 2017, doi: 10.1038/ncomms15257.

[10] X. Tang, M. M. Ackerman, M. Chen, and P. Guyot-Sionnest, “Dual-band infrared imaging using stacked colloidal quantum dot photodiodes,” *Nat. Photonics*, vol. 13, no. 4, pp. 277–282, Apr. 2019, doi: 10.1038/s41566-019-0362-1.

[11] M. M. Ackerman, X. Tang, and P. Guyot-Sionnest, “Fast and Sensitive Colloidal Quantum Dot Mid-Wave Infrared Photodetectors,” *ACS Nano*, vol. 12, no. 7, pp. 7264–7271, Jul. 2018, doi: 10.1021/acsnano.8b03425.

[12] G. Shen, M. Chen, and P. Guyot-Sionnest, “Synthesis of Nonaggregating HgTe Colloidal Quantum Dots and the Emergence of Air-Stable n-Doping,” *J. Phys. Chem. Lett.*, vol. 8, no. 10, pp. 2224–2228, May 2017, doi: 10.1021/acs.jpclett.7b00775.

[13] S. Keuleyan, E. Lhuillier, and P. Guyot-Sionnest, “Synthesis of Colloidal HgTe Quantum Dots for Narrow Mid-IR Emission and Detection,” *J. Am. Chem. Soc.*, vol. 133, no. 41, pp. 16422–16424, Oct. 2011, doi: 10.1021/ja2079509.

[14] H. Sun, F. Wang, and W. E. Buhro, “Tellurium Precursor for Nanocrystal Synthesis: Tris(dimethylamino)phosphine Telluride,” *ACS Nano*, vol. 12, no. 12, pp. 12393–12400, Dec. 2018, doi: 10.1021/acsnano.8b06468.

[15] M. Born and R. Oppenheimer, “Zur Quantentheorie der Molekeln,” *Annalen der Physik*, vol. 389, no. 20, pp. 457–484, 1927, doi: 10.1002/andp.19273892002.

[16] D. R. Hartree, “The Wave Mechanics of an Atom with a Non-Coulomb Central Field. Part I. Theory and Methods,” *Mathematical Proceedings of the Cambridge Philosophical Society*, vol. 24, no. 1, pp. 89–110, Jan. 1928, doi: 10.1017/S0305004100011919.

[17] J. C. Slater, “The Theory of Complex Spectra,” *Physical Review*, vol. 34, pp. 1293–1322, Nov. 1929, doi: 10.1103/PhysRev.34.1293.

[18] V. Fock, “Näherungsmethode zur Lösung des quantenmechanischen Mehrkörperproblems,” *Z. Physik*, vol. 61, no. 1, pp. 126–148, Jan. 1930, doi: 10.1007/BF01340294.

[19] M. L. Boas, *Mathematical Methods in the Physical Sciences*. Wiley, 2005.

[20] P. Hohenberg and W. Kohn, “Inhomogeneous Electron Gas,” *Phys. Rev.*, vol. 136, no. 3B, pp. B864–B871, Nov. 1964, doi: 10.1103/PhysRev.136.B864.

[21] F. Giustino, *Materials Modelling Using Density Functional Theory: Properties and Predictions*. Oxford, UNITED KINGDOM: Oxford University Press, 2014.

[22] T. Tsuneda, “Exchange-Correlation Functionals,” in *Density Functional Theory in Quantum Chemistry*, T. Tsuneda, Ed., Tokyo: Springer Japan, 2014, pp. 101–124. doi: 10.1007/978-4-431-54825-6_5.

[23] “ENCUT - VASP Wiki.” Accessed: Jun. 17, 2024. [Online]. Available: https://www.vasp.at/wiki/index.php/ENCUT

[24] “Category:Pseudopotentials - VASP Wiki.” Accessed: Jun. 17, 2024. [Online]. Available: https://www.vasp.at/wiki/index.php/Category:Pseudopotentials

[25] R. P. Feynman, “Forces in Molecules,” *Phys. Rev.*, vol. 56, no. 4, pp. 340–343, Aug. 1939, doi: 10.1103/PhysRev.56.340.

[26] "POTIM - VASP Wiki." Accessed: Jun. 19, 2024. [Online]. Available: https://www.vasp.at/wiki/index.php/POTIM

[27] W. H. Press, *Numerical Recipes 3rd Edition: The Art of Scientific Computing*. Cambridge University Press, 2007.

[28] R. Fletcher and C. M. Reeves, "Function minimization by conjugate gradients," *The Computer Journal*, vol. 7, no. 2, pp. 149–154, Jan. 1964, doi: 10.1093/comjnl/7.2.149.

[29] E. Polak and G. Ribiere, "Note sur la convergence de méthodes de directions conjuguées," *R.I.R.O.*, vol. 3, no. 16, Art. no. 16, 1969, doi: 10.1051/m2an/196903R100351.

[30] "EDIFFG - VASP Wiki." Accessed: Jun. 19, 2024. [Online]. Available: https://www.vasp.at/wiki/index.php/EDIFFG

[31] N. M. Stuart and K. Sohlberg, "A method of calculating surface energies for asymmetric slab models," *Phys. Chem. Chem. Phys.*, vol. 25, no. 19, pp. 13351–13358, May 2023, doi: 10.1039/D2CP04460A.

[32] X. Tian, T. Wang, L. Fan, Y. Wang, H. Lu, and Y. Mu, "A DFT based method for calculating the surface energies of asymmetric MoP facets," *Applied Surface Science*, vol. 427, pp. 357–362, Jan. 2018, doi: 10.1016/j.apsusc.2017.08.172.

[33] "POSCAR - VASP Wiki." Accessed: Jun. 19, 2024. [Online]. Available: https://www.vasp.at/wiki/index.php/POSCAR

[34] A. J. Houtepen, Z. Hens, J. S. Owen, and I. Infante, "On the Origin of Surface Traps in Colloidal II–VI Semiconductor Nanocrystals," *Chem. Mater.*, vol. 29, no. 2, pp. 752–761, Jan. 2017, doi: 10.1021/acs.chemmater.6b04648.

[35] S. Yang, D. Dardzinski, A. Hwang, D. I. Pikulin, G. W. Winkler, and N. Marom, "First-principles feasibility assessment of a topological insulator at the InAs/GaSb interface," *Phys. Rev. Mater.*, vol. 5, no. 8, p. 084204, Aug. 2021, doi: 10.1103/PhysRevMaterials.5.084204.

[36] J. J. Jorgensen and G. L. W. Hart, "Effectiveness of smearing and tetrahedron methods: best practices in DFT codes," *Modelling Simul. Mater. Sci. Eng.*, vol. 29, no. 6, p. 065014, Jul. 2021, doi: 10.1088/1361-651X/ac13ca.

[37] G. Kresse and J. Furthmüller, "Efficiency of ab-initio total energy calculations for metals and semiconductors using a plane-wave basis set," *Computational Materials Science*, vol. 6, no. 1, pp. 15–50, Jul. 1996, doi: 10.1016/0927-0256(96)00008-0.

[38] N. Kirkwood *et al.*, “Finding and Fixing Traps in II–VI and III–V Colloidal Quantum Dots: The Importance of Z-Type Ligand Passivation,” *J. Am. Chem. Soc.*, vol. 140, no. 46, pp. 15712–15723, Nov. 2018, doi: 10.1021/jacs.8b07783.

[39] C. Freysoldt *et al.*, “First-principles calculations for point defects in solids,” *Rev. Mod. Phys.*, vol. 86, no. 1, pp. 253–305, Mar. 2014, doi: 10.1103/RevModPhys.86.253.

[40] E. A. Moelwyn-Hughes, *The Kinetics of Reactions in Solution*. Clarendon Press, 1933.

[41] W. Yan, X. Yuan, and X. Liu, “Theoretical investigation of dissociative and non-dissociative acetic-acid on TiO2-B surfaces,” *Applied Surface Science*, vol. 494, pp. 850–858, Nov. 2019, doi: 10.1016/j.apsusc.2019.07.198.

[42] A. Svane, N. E. Christensen, M. Cardona, A. N. Chantis, M. van Schilfgaarde, and T. Kotani, “Quasiparticle band structures of β-HgS, HgSe, and HgTe,” *Phys. Rev. B*, vol. 84, no. 20, p. 205205, Nov. 2011, doi: 10.1103/PhysRevB.84.205205.